Doctoral Dissertations   Graduate School

8-2012

Measurement Of Power-law Creep Parameters By Instrumented Indentation Methods

Caijun Su
csu2@utk.edu

To the Graduate Council:

I am submitting herewith a dissertation written by Caijun Su entitled "Measurement Of Power-law Creep Parameters By Instrumented Indentation Methods." I have examined the final electronic copy of this dissertation for form and content and recommend that it be accepted in partial fulfillment of the requirements for the degree of Doctor of Philosophy, with a major in Materials Science and Engineering.

George M. Pharr, Major Professor

We have read this dissertation and recommend its acceptance:

Warren C. Oliver, Dayakar Penumadu, Yanfei Gao

Accepted for the Council:
Dixie L. Thompson

Vice Provost and Dean of the Graduate School

(Original signatures are on file with official student records.)

Measurement Of Power-law Creep Parameters By Instrumented Indentation Methods

**A Dissertation Presented for the
Degree of Doctor of Philosophy
The University of Tennessee, Knoxville**

**Caijun Su
August 2012**

DEDICATION

To my parents, Su, Yongbin and Liao, Huilan for their love, endless support and encouragement.

ACKNOWLEDGEMENTS

ABSTRACT

New experimental methods have been developed to measure the uniaxial power-law creep parameters α [alpha] and n in the relation $\dot{\varepsilon}$[epsilon dot] $= \alpha$[alpha]σ^n[sigma] ($\dot{\varepsilon}$ [epsilon dot] is the creep strain rate and σ [sigma] is the creep stress) from the load, time, displacement and stiffness data recorded during an instrumented indentation experiment performed with a conical or pyramidal indenter. The methods are based on an analysis of Bower et al., which relates the indentation creep rate to the uniaxial creep parameters based on simple assumptions about the constitutive behavior (Bower et al., 1993). Using finite element simulations to establish the influences of finite deformation and transients caused by elasticity, the proposed methods are explored experimentally using amorphous selenium as a model material. Cylindrical specimens compressed at high temperatures and low strain rates deformed stably into barrel-like shapes, while tests at low temperatures and high strain rates caused the sample to catastrophically shatter. These observations are consistent with the stress exponent and kinetic activation parameters extracted from the nanoindentation creep tests. With a few notable exceptions, the values of both α [alpha] and n derived from the indentation data at 35 ℃ [Celsius] are generally in good agreement with those measured in uniaxial compression, thus demonstrating the validity of the approach. Another technique, based on the measured elastic contact stiffness and assumed values of Young's modulus and Poisson's ratio, is proposed as an alternative method to extract α [alpha] and n when the affect of thermal drift is such that the measured displacement in the indentation test is no longer reliable. Experimental verification of the stiffness method is provided through constant load and hold indentation creep experiments performed with a Berkovich indenter on amorphous selenium at 35 ℃ [Celsius], where the affect of drift is extremely small, and high purity polycrystalline aluminum at 250 ℃ [Celsius], where the affect of drift is so strong that the measured displacement is completely useless. Results show that the stiffness method can accurately predict the projected contact area and α [alpha] and n for both materials, thus demonstrating the validity of the proposed stiffness method.

TABLE OF CONTENTS

LIST OF TABLES

LIST OF FIGURES

ix

INTRODUCTION

This dissertation is based on three journal articles: 1) "Plastic instability in amorphous selenium near its glass transition temperature"; 2) "Measurement of power-law creep parameters by instrumented indentation methods"; and 3) "An experimental method for eliminating thermal drift from instrumented indentation creep experiments". The focus of these articles is the utilization of instrumented indentation techniques specifically designed to measure uniaxial power-law creep properties based on an analysis of Bower et al. (Bower et al., 1993). The first article was published in the *Journal of Materials Research* in 2010; the second article was submitted to the *Journal of the Mechanics and Physics of Solids* on March 1st, 2012; and the third article will be submitted to the *Journal of Materials Research*. In keeping with the guidelines for multi-part dissertation by the Graduate School of the University of Tennessee, each article is presented as an individual chapter in the dissertation, while the figures and tables are listed in an appendix at the end of each chapter.

Creep is time-dependent permanent deformation that occurs when materials experience long-term exposure to stress, particularly at high homologous temperatures. Creep deformation occurs in nearly all classes of materials. In applications requiring a high degree of dimensional stability, creep can be the key element that determines a material's ability to meet specific design goals. Creep is a complex phenomenon that occurs in different stages that are driven by numerous mechanisms that depend on stress, temperature, and microstructure. The most well understood stage of creep is secondary or steady-state creep, where the strain rate becomes nearly constant with time as the rate of work hardening and recovery effectively balance one another. For uniaxial tests, steady state creep rates, $\dot{\varepsilon}$, are usually related to the uniaxial creep stress, σ, through the simple power law relation

$$\dot{\varepsilon} = \alpha\sigma^n \, , \tag{1}$$

where α and n are material parameters - a pre-exponential term called the creep coefficient, and the stress or creep exponent, respectively. Uniaxial tension and compression are the testing techniques most commonly used to determine α and n.

1

These techniques can be impractical and even impossible, however, in applications limited to volumes of material on the micron scale, such as thin films, solder joints and metallization lines. While instrumented indentation is ideally suited to investigate the mechanical behavior of small volumes of materials, a thorough understanding of the relationship between the uniaxial constitutive creep parameters (α and n) and the load, displacement, and time data recorded during an indentation experiment is not well understood because of the complex nature of stress and strain rate history during indentation contact (Asif and Pethica, 1997; Bucaille et al., 2002; Chu and Li, 1977; Grau et al., 1998; Li and Ngan, 2004; Lucas and Oliver, 1999; Lucas and Pendleton, 1982; Mayo and Nix, 1988; Oliver and Pharr, 1992; Poisl et al., 1995; Raman and Berriche, 1992; Su et al., 2010; Wang et al., 2010; Wang et al., 2009; Wilkinson and Ashby, 1975).

The constitutive relationship between strain rate and stress in an indentation test is also expressed as a power law. Adopting the nomenclature of Bower et al., the stress, p, in an indentation test should be related to the pressure exerted by the indenter, $p=P/A$, where P is the applied load and A is some appropriate measure of the area of the indentation contact (the exact definition of this area will be examined in the second article) (Bower et al., 1993). Accordingly, the indentation strain rate, $\dot{\varepsilon}_i$, should be directly related to $\dot{h}/h$, where $\dot{h}$ is the indentation displacement rate. Therefore, the indentation strain rates, $\dot{\varepsilon}_i$, are related to the indentation contact pressure, p, through a power law relation equivalent to Eq. 1 of the form:

$$\dot{\varepsilon}_i = \left(\frac{1}{h}\right)\left(\frac{dh}{dt}\right) = \beta p^n, \tag{2}$$

where β is the indentation creep coefficient and n is the stress or creep exponent. While previous instrumented indentation studies have shown good correlation between the creep exponent, n, measured in uniaxial compression and indentation, there is very little experimental data in the literature investigating the correlation between the creep coefficient, α, measured in uniaxial tension or compression and the creep coefficient, β, measured in instrumented indentation (Lucas and Oliver, 1999; Mayo and Nix, 1988; Raman and Berriche, 1992). Thus, in order to fully characterize the uniaxial creep

2

parameters in an instrumented indentation test, one must also be able to relate β to α. Theoretical modeling and numerical simulation techniques are frequently used to correlate the constitutive behavior of materials in uniaxial tension or compression to the load, displacement, and time data recorded during an instrumented indentation test (Atkins et al., 1966; Bower et al., 1993; Bucaille et al., 2002; Cheng, 2001; Fischer-Cripps, 2004; Hill, 1992; Lee et al., 2010; Mulhearn and Tabor, 1960; Ogbonna et al., 1995; Sargent and Ashby, 1992; Storakers and Larsson, 1994; Yang et al., 1995). However, these correlations are often limited in applicability based on the assumptions used in the models and simulations.

Indentation creep experiments are often performed with localized heating stages in order to achieve high homologous temperatures in the sample. When the tip and sample are not maintained at the same constant temperature, the measured displacement may not be reliable due to dimensional instabilities in the sample and instrument that are caused by the lack of thermal equilibrium. Any contribution from thermal drift to the measured displacement can only be accurately accounted for if the drift rate is constant over the duration of the test. When these criteria cannot be met, the error in the measured displacement directly manifests itself as an error in the predicted creep properties. The continuous stiffness measurement (CSM) technique is not sensitive to thermal drift because the system operates on a time scale, 45 Hz, which is substantially faster than the rate at which nominal drift rates can affect the measured displacement. (Asif and Pethica, 1997; Goldsby et al., 2004; Hay et al., 2010; Li and Bhushan, 2002; Oliver and Pharr, 1992, 2004; Rar et al., 2005). Because of this, the CSM technique can reliably determine the elastic contact stiffness with little or no error caused by thermal drift. With this technique, the elastic contact stiffness is measured as a continuous function of depth by utilizing a frequency-specific phase-lock amplifier (PLA), which superimposes a small dynamic oscillation on the load signal and measures the resulting amplitude and phase shift of the displacement signal. With a knowledge of the sample's Young's modulus and Poisson's ratio, Sneddon's stiffness equation and the measured stiffness can be used to determine the contact area and ultimately the strain rate and stress in a manner that is largely independent of thermal drift (Sneddon, 1965).

3

The goal of the work in this dissertation was to develop techniques by which one can measure the uniaxial power-law creep properties by instrumented indentation techniques based on Bower's analysis, which relates the indentation creep rate to the uniaxial creep parameters based on simple assumptions about the constitutive behavior (Bower et al., 1993). The first paper investigates the deformation behavior of amorphous selenium near its glass transition temperature (31°C) by uniaxial compression and nanoindentation creep tests. Selenium is a suitable model material for this work because its glass transition temperature, T_g, is 31.0 ± 0.5 °C, and it creeps in very well defined way at slightly higher temperatures (e.g., 35 °C) (Poisl et al., 1995). Thus, simple modifications of commercially available indentation and uniaxial tension/compression systems could be used to characterize the creep behavior without the complications of conducting very high temperature tests. Similarity contact analysis is used to extract the creep exponent, n, and the kinetic activation volume, Ω, from nanoindentation creep tests which are correlated with the ductile-to-brittle transition observed in compression testing on amorphous selenium at 25-40 °C. The second paper focuses on the development of experimental techniques and analysis methods to measure the uniaxial power-law creep parameters α and n in the relation $\dot{\varepsilon} = \alpha \sigma^n$ ($\dot{\varepsilon}$ is the creep strain rate and σ is the creep stress) from indentation data obtained with a conical or pyramidal indenter. Using finite element simulations to establish the influences of finite deformation and transients caused by elasticity, the proposed methods are explored experimentally on amorphous selenium with a Berkovich indenter using three different loading methods. The third paper utilizes Bower's analysis and Sneddon's indentation stiffness equation to provide an alternative method for determining the uniaxial power law creep parameters, α and n, when the displacement data are deemed unreliable due to thermal drift. Experimental verification of the alternative method was conducted on amorphous selenium at 35 °C, in which the effects of thermal drift are minimal and the method can be checked against the measure displacements, and high purity polycrystalline aluminum at 250 °C, in which thermal drift effects are enormous and the measured displacements cannot be used to determine creep rates.

References

Asif, S.A.S., Pethica, J.B., 1997. Nanoindentation creep of single-crystal tungsten and gallium arsenide. Philos. Mag. A-Phys. Condens. Matter Struct. Defect Mech. Prop. 76, 1105-1118.

Atkins, A.G., Silverio, A., Tabor, D., 1966. Indentation hardness and creep of solids. Journal of the Institute of Metals 94, 369-378.

Bower, A.F., Fleck, N.A., Needleman, A., Ogbonna, N., 1993. Indentation of a power law creeping solid. Proc. R. Soc. London Ser. A-Math. Phys. Eng. Sci. 441, 97-124.

Bucaille, J.L., Felder, E., Hochstetter, G., 2002. Identification of the viscoplastic behavior of a polycarbonate based on experiments and numerical modeling of the nano-indentation test. J. Mater. Sci. 37, 3999-4011.

Cheng, Y.T., 2001. Scaling relationships in indentation of power-law creep solids using self-similar indenters. Philos. Mag. Lett. 81, 9-16.

Chu, S.N.G., Li, J.C.M., 1977. Impression creep - new creep test. J. Mater. Sci. 12, 2200-2208.

Fischer-Cripps, A.C., 2004. A simple phenomenological approach to nanoindentation creep. Mater. Sci. Eng. A-Struct. Mater. Prop. Microstruct. Process. 385, 74-82.

Goldsby, D.L., Rar, A., Pharr, G.M., Tullis, T.E., 2004. Nanoindentation creep of quartz, with implications for rate- and state-variable friction laws relevant to earthquake mechanics. J. Mater. Res. 19, 357-365.

Grau, P., Berg, G., Meinhard, H., Mosch, S., 1998. Strain rate dependence of the hardness of glass and Meyer's law. J. Am. Ceram. Soc. 81, 1557-1564.

Hay, J., Agee, P., Herbert, E., 2010. Continuous stiffness measurement during instrumented indentation testing. Exp. Tech. 34, 86-94.

Hill, R., 1992. Similarity analysis of creep indentation tests. Proc. R. Soc. London Ser. A-Math. Phys. Eng. Sci. 436, 617-630.

Lee, J.H., Zhou, C., Su, C.J., Gao, Y.F., Pharr, G.M., 2010. Similarity Relationships in Creep Contacts and Applications in Nanoindentation Tests. Mat. Res. Soc. Symp. Proc. 1224, FF07-08.

Li, H., Ngan, A.H.W., 2004. Size effects of nanoindentation creep. J. Mater. Res. 19, 513-522.

Li, X.D., Bhushan, B., 2002. A review of nanoindentation continuous stiffness measurement technique and its applications. Mater. Charact. 48, 11-36.

Lucas, B.N., Oliver, W.C., 1999. Indentation power-law creep of high-purity indium. Metall. Mater. Trans. A-Phys. Metall. Mater. Sci. 30, 601-610.

Lucas, G.E., Pendleton, C., 1982. Time-dependent flow properties from indentation tests. J. Nucl. Mater. 103, 1539-1543.

Mayo, M.J., Nix, W.D., 1988. A micro-indentation study of superplasticity in Pb, Sn, and Sn-38 wt-percent-Pb. Acta Metallurgica 36, 2183-2192.

Mulhearn, T.O., Tabor, D., 1960. Creep and hardness of metals - a physical study. Journal of the Institute of Metals 89, 7-12.

Ogbonna, N., Fleck, N.A., Cocks, A.C.F., 1995. Transient creep analysis of ball indentation. Int. J. Mech. Sci. 37, 1179-1202.

Oliver, W.C., Pharr, G.M., 1992. An improved technique for determining hardness and elastic-modulus using load and displacement sensing indentation experiments. J. Mater. Res. 7, 1564-1583.

Oliver, W.C., Pharr, G.M., 2004. Measurement of hardness and elastic modulus by instrumented indentation: Advances in understanding and refinements to methodology. J. Mater. Res. 19, 3-20.

Poisl, W.H., Oliver, W.C., Fabes, B.D., 1995. The relationship between indentation and uniaxial creep in amorphous selenium. J. Mater. Res. 10, 2024-2032.

Raman, V., Berriche, R., 1992. An investigation of the creep processes in tin and aluminum using a depth-sensing indentation technique. J. Mater. Res. 7, 627-638.

Rar, A., Sohn, S., Oliver, W.C., Goldsby, D.L., Tullis, T.E., Pharr, G.M., 2005. On the measurement of creep by nanoindentation with continuous stiffness techniques. Mater. Res. Soc. Symp. Proc. 841, 119-124.

Sargent, P.M., Ashby, M.F., 1992. Indentation creep. Mater. Sci. Technol. 8, 594-601.

Sneddon, I.N., 1965. The relation between load and penetration in the axisymmetric Boussinesq problem for a punch of arbitrary profile. Int. J. Eng. Sci. 3, 47.

Storakers, B., Larsson, P.L., 1994. On brinell and boussinesq indentation of creeping solids. J. Mech. Phys. Solids 42, 307-332.

Su, C.J., LaManna, J.A., Gao, Y.F., Oliver, W.C., Pharr, G.M., 2010. Plastic instability in amorphous selenium near its glass transition temperature. J. Mater. Res. 25, 1015-1019.

Wang, C.L., Lai, Y.H., Huang, J.C., Nieh, T.G., 2010. Creep of nanocrystalline nickel: A direct comparison between uniaxial and nanoindentation creep. Scr. Mater. 62, 175-178.

Wang, C.L., Zhang, M., Nieh, T.G., 2009. Nanoindentation creep of nanocrystalline nickel at elevated temperatures. J. Phys. D-Appl. Phys. 42, 115405.

Wilkinson, D.S., Ashby, M.F., 1975. Pressure sintering by power law creep. Acta Metallurgica 23, 1277-1285.

Yang, F.Q., Li, J.C.M., Shih, C.W., 1995. Computer-simulation of impression creep using the hyperbolic sine stress law. Mater. Sci. Eng. A-Struct. Mater. Prop. Microstruct. Process. 201, 50-57.

.

CHAPTER I
Plastic instability in amorphous selenium near its glass transition temperature

A version of this chapter was originally published by C.J. Su, J.A. LaManna, Y.F. Gao, W.C. Oliver, and G.M. Pharr in 2010:

Authors:

C.J. Su, J.A. LaManna
Dept. of Materials Science and Engineering, University of Tennessee, Knoxville, TN 37996

Y.F. Gao
Dept. of Materials Science and Engineering, University of Tennessee, Knoxville, TN 37996; and Computer Science and Mathematics Division, Oak Ridge National Lab, Oak Ridge, TN 37831

W.C. Oliver
Nanomechanics Inc., Oak Ridge, TN 37830

G.M. Pharr
Dept. of Materials Science and Engineering, University of Tennessee, Knoxville, TN 37996; and Materials Science and Technology Division, Oak Ridge National Lab, Oak Ridge, TN 37831

C.J. Su's involvement in the article: prepared the samples, designed and performed indentation creep experiments, analyzed the experimental data, built theoretical models to explain the experimental data, wrote and revised the article.

Co-researchers' contributions are listed as follows:

J.A. LaManna performed uniaxial compression creep experiments.

Y.F. Gao worked with Caijun to build theoretical models to explain the experimental data, prepare and revise the article.

W.C. Oliver provided technical support and worked with Caijun to analyze the experimental data.

 G.M. Pharr provided research guideline and worked with Caijun to analyze the experimental data.

Abstract

The deformation behavior of amorphous selenium near its glass transition temperature (31 ℃) has been investigated by uniaxial compression and nanoindentation creep tests. Cylindrical specimens compressed at high temperatures and low strain rates deform stably into barrel-like shapes, while tests at low temperatures and high strain rates lead to fragmentation. These results agree well with stress exponent and kinetic activation parameters extracted from nanoindentation creep tests using a similarity analysis. The dependence of the deformation modes on temperature and strain rate can be understood as a consequence of material instability and strain localization in rate-dependent solids.

1.   Introduction

Amorphous materials usually display a ductile-to-brittle transition with a decrease of the temperature, with the transition temperature depending on the applied strain rate. While tensile/compression tests are commonly used to characterize such behavior, the use of novel small-scale mechanical testing methods such as the nanoindentation may in some instances have distinct advantages, since the highly constrained deformation during indentation suppresses fracture and allows other deformation processes to be observed and measured (Gao et al., 2006; Oliver and Pharr, 1992). Indentation testing, however, produces a much more complex stress state and strain rate history, so that the analysis of rate-dependent material behavior is not straightforward. The primary objective of this work was to determine whether the kinetic activation parameters obtained from indentation creep tests can be correlated with the ductile-to-brittle transition observed in compression testing. To this end, a comparative study of uniaxial compression and nanoindentation creep tests was conducted on amorphous selenium. This material was chosen because its glass transition temperature, T_g $=31.0\pm0.5\,℃$, is near room temperature, so that simple modifications of a standard nanoindentation system can be used to explore the deformations behavior above and below T_g (LaManna, 2006; Poisl et al., 1995; Tang and Ngan, 2005).

2.   Preliminaries

The Oliver-Pharr method for determining elastic modulus and indentation hardness is based on an analysis of rate-independent elastic-plastic contact, for which the correlation between the strain hardening characteristics and the indentation response is well established (Oliver and Pharr, 1992). Here, we focus on the behavior of a rate-dependent solid and how the indentation load, displacement, and their rates can be appropriately normalized so that creep constitutive parameters can be extracted (Bower et al., 1993; Liu et al., 2008; Lucas and Oliver, 1999; Mayo and Nix, 1988). Following the

similarity analysis in Bower et al., we note that for a pure creeping solid without strain hardening (thus excluding primary creep behavior), at any particular instant, the strain rates and stresses are independent of the loading history and depend only on the instantaneous velocities and contact radius prescribed on the surface (Bower et al., 1993). Consequently, the instantaneous strain rate and stress fields are identical to those under a rigid flat punch of radius a which indents a creeping half-space at a velocity $\dot{h}$, where h is the indentation depth. For a power-law creeping solid, as defined by $\sigma/\sigma_0 = \left(\dot{\varepsilon}/\dot{\varepsilon}_0\right)^{1/n}$ with reference stress σ_0, reference strain rate $\dot{\varepsilon}_0$, and stress exponent n, the indentation load P is related to the effective strain rate $\dot{h}/a$ by $\dfrac{P}{\pi a^2 \sigma_0} = F_a \left(\dfrac{\dot{h}}{a\dot{\varepsilon}_0}\right)^{1/n}$, where the dimensionless number F_a is a function of n. The relationship between a and h, which is determined by the geometry of the indenter, is independent of the contact history. For a cone with the half included angle β, the relationship is given simply by $h = \frac{a}{c\tan\beta}$, where the dimensionless number c is a function of n and provides a direct measure of the amount of pile-up or sink-in relative to the original, undeformed surface. Consequently, for the Berkovich-equivalent cone (i.e., $\beta = 70.3°$), we get

$$\frac{P}{\pi a^2 \sigma_0} = \alpha\left(\frac{\dot{h}/h}{\dot{\varepsilon}_0}\right)^{1/n}, \quad \alpha = \frac{F_a(n)}{\left[c(n)\tan\beta\right]^{1/n}}. \tag{1}$$

Here, the new dimensionless parameter α is a monotonically increasing function of n. When $n = 1$, the material is a Newtonian viscous solid and $\alpha = \frac{4}{3\tan\beta}$. When $n \to \infty$, the material approaches the rate-independent limit, so that $\alpha = \frac{P}{\pi a^2 \sigma_0}$ is the constraint factor, being about 3 for a blunt indenter (Bower et al., 1993). For the purposes of analysis, we define a nominal hardness by $H = \frac{P}{\pi(h\tan\beta)^2}$, where $\pi(h\tan\beta)^2$ is the projected contact area. Consequently,

$$\frac{H}{\sigma_0} = \alpha^*\left(\frac{\dot{h}}{h\dot{\varepsilon}_0}\right)^{1/n}, \tag{2}$$

12

where $\alpha^* = c^2\alpha$. This dimensionless number monotonically increases from about 0.2 to 5 as *n* increases from unity to infinity (Bower et al., 1993). The nominal hardness, which differs from the true hardness in that it ignores the effects of pile-up and sink-in, is experimentally convenient since it can be determined directly from load-displacement-time data obtained in an indentation creep test.

3.   Experimental procedures

Amorphous selenium samples were prepared by melting pure amorphous selenium shot (Alfa Aesar, Ward Hill, MA) and quenching into copper molds. The as-cast samples for nanoindentation (31.75mm in diameter by 5mm thick) had a mirror surface finish and were thus ready for indentation experiments after being affixed to an aluminum mounting stub with Crystalbond (Electron Microscopy Sciences, Hatfield, PA). Nanoindentation tests were performed using a MTS Nano Indenter XP (MTS Nano Instruments, Oak Ridge, TN) equipped with a Berkovich indenter. Inside the indenter chamber, a 250W lamp was mounted beneath the frame of the vibration isolation table. The temperature in the chamber was controlled to within 0.001℃ resolution and 0.01℃ precision by a proportional temperature controller that regulated the amount of power supplied to the lamp based on feedback from a precision platinum thermometer. Two small fans inside the housing mixed the air to maintain uniform heat distribution. An aluminum heat shield was placed directly below the vibration isolation table to minimize direct heating from the lamp. At each temperature, four creep tests were conducted with a Berkovich indenter using a constant load-and-hold method in which the indenter was loaded to a prescribed maximum load (e.g., 1mN, 10mN, 100mN, and 500mN) in two seconds and then held for an hour or until a maximum depth of 50µm was achieved.

Cast cylindrical samples for compression testing (10mm in diameter and 20mm long) were polished on both ends to ensure conforming contact with the compression platens. Uniaxial compression tests were performed using a MTS 10/GL screw driven uniaxial tension/compression testing machine (Eden Prairie, MN) equipped with an

environmental chamber with a temperature control system similar to that used in the nanoindentation tests.

4.   Results and discussion

As shown in Fig. 1.1 (a), compressed specimens either deformed stably into a barrel-like shape at low strain rates and high temperatures or fragmented into small pieces at high strain rates and low temperatures (note that figures and tables appear in appendices). Plotted on the temperature (T) versus strain rate ($\dot{\varepsilon}$) map, the boundary between these two deformation modes is delineated with a positive slope of $d\dot{\varepsilon}/dT$. Fragmentation was preceded by an inhomogeneous deformation mode in which the strain fields were localized into narrow shear bands, as will be discussed later.

The aforementioned analysis lays the theoretical foundation for our nanoindentation creep measurements. When the constant load-and-hold method is applied, the displacement-time curve can be used to extract the stress exponent, since integration of Eq. 2 with *P=constant* yields $h \propto t^{1/2n}$. However, this procedure should be used only for displacement data that are larger than several times of $h_{elastic} = \sqrt{\frac{\pi P}{2\tan\beta E^*}}$, where E^* is the effective indentation modulus, in order to avoid elastic influences on the measured displacements (Gao et al., 2008). This condition is satisfied in our analysis. For instance, when P=10mN, $h_{elastic}$~0.75 μm, while we take $h>2$ μm in our data analysis. Using this procedure, the stress exponent measured from indentation creep tests of amorphous selenium is plotted against $\dot{\varepsilon}_{eff} = \dot{h}/h$ in Fig. 1.2 (a). Since the dependence on the applied load is weak, it is possible to extract values of the stress exponent and plot n contours on a $(T, \dot{h}/h)$ map, as has been done for a 10mN load in Fig. 1.3 (a). At high temperatures and low strain rates, the deformation behavior is Newtonian viscous flow with n approaching unity. The n contours nicely follow the boundary of the two deformation modes in Fig. 1.1 (b). If we take the *n*~2 contour in Fig. 1.3 (a) as the transition boundary and compare it to the dashed line in Fig. 1.1 (b), we can see the same

14

qualitative trend, but the strain rate may vary by one or two orders of magnitude. It should be noted that the connection between the indentation strain rate and compression strain rate has not been fully established, which will be an ideal research task for amorphous selenium samples (Poisl et al., 1995; Wang et al., 2009). A possible size effect, as reported in the indentation creep tests by Li and Ngan, may not occur in our results, because the difference between P=10mN and P=100mN in Fig. 1.2 is small, and the deformation mechanisms of amorphous materials do not seem to have a micrometer length scale due to the lack of material microstructure and dislocation-like defects (Li and Ngan, 2004).

One can also use the data to measure the activation volume, $\Omega = k_B T \frac{\partial \ln \dot{\varepsilon}}{\partial \tau_{eff}}\Big|_T$, provided there is an appropriate choice of the effective shear stress, τ_{eff}. While many previous works have used a fixed constraint factor of 3 to relate the hardness to the effective Mises stress, the analysis leading to Eq. (2) suggests that we use the factor of α^* instead, which is not constant but depends on n (Lucas and Oliver, 1999; Wang et al., 2009). Accordingly, we assume that $\tau_{eff} = \frac{H}{\sqrt{3}\alpha^*}$, where the factor $\sqrt{3}$ relates the Mises stress to the shear stress. From $n = \frac{\partial \ln \dot{\varepsilon}}{\partial \ln \tau_{eff}}\Big|_T$, we get $\Omega = n k_B T / \tau_{eff}$, implying that the activation volume can be experimentally evaluated from the data in Fig. 1.2. At 40 ℃, the indentation hardness is 0.0005~0.1GPa, and the compression flow stress is 0.001~0.03GPa. At 25 ℃, the hardness is 0.1~0.4GPa, and the flow stress is 0.05~0.4GPa. The contour plots in Fig. 1.3 (b) show that Ω increases rapidly as the temperature increases and the strain rate decreases, which agrees well with the observations in Fig. 1.1 (b) and the contours in Fig. 1.3 (a). A previous study also shows that the activation volume increases with respect to the temperature.[4] However, their reported activation volume magnitude is about two orders of magnitude smaller than our results, which is probably due to the different choices of effective stress. It should also be pointed out that the activation volume gradient is large at high temperatures in Fig. 1.3

(b), while a logarithmic plot of activation volume will show a clear gradient near the glass transition temperature.

The relationship between the kinetic activation parameter and deformation modes can be understood by material instability in rate-dependent plastic solids (Needleman, 1988; Rice, 1977; Rudnicki and Rice, 1975). Under certain conditions (e.g., a strain softening material behavior), a smoothly varying strain field can evolve into narrow bands inside of which the shear strain fields localize and outside of which the shear strains are almost negligible. Shear fracture will then occur at the shear localization sites. For rate-independent plastic solids, the necessary condition for strain localization corresponds to the loss of ellipticity of the equations governing incremental equilibrium, or equivalently, the singularity of the acoustic tensor (i.e., projected material tangent modulus on a given shear-band plane) (Rice, 1977; Rudnicki and Rice, 1975). In this case, the temperature dependence of deformation modes arises only from the contribution of thermal effects in the constitutive laws. On the other hand, material instability in rate-dependent plastic solids is manifested by spectral growth of the strain field (Needleman, 1988). In this case, initial imperfections or small spatial fluctuations in the strain field gradually grow into a spatial distribution that consists of high strains in certain locations and low strains elsewhere, and this strain localization process can be significantly delayed by the material rate sensitivity. Since the activation volume characterizes the thermally activated process for plastic flow, when Ω is large, a large spatial variation is required for the inhomogeneous deformation to develop, which is difficult to achieve. When Ω is small, a large stress is needed to accommodate the applied strain rate field, and a short-wavelength perturbation can quickly grow into large strains. This establishes the correspondence between deformation modes and kinetic activation parameters.

The aforementioned line of argument does not require a detailed picture of the atomistic scale deformation mechanism. That is, the dependence of activation volume on temperature and strain rate needs a physical model. Nevertheless, insights into the mechanism can be obtained from the positive slopes of the activation volume contours, which suggest the operation of a diffusion-like process for structural relaxation. At high temperature and low strain rate, structural fluctuations, especially the short-wavelength

16

ones, can be easily annihilated by such a diffusional process because of higher atomic mobility and long time for diffusion to proceed, thus promoting homogenous deformation. This observation agrees well with the free volume or the shear transformation zone (STZ) theories for deformation of amorphous alloys (Argon, 1979; Gao, 2006; Gao et al., 2007; Spaepen, 1977; Yang et al., 2007). The STZ volume is roughly the product of the activation volume and the elastic limit strain (Pan et al., 2008). Consequently, measurements of Ω contours may also be used to understand the brittle-to-ductile transition in these materials.

5. Summary and conclusions

In summary, a correlation between uniaxial compression tests and nanoindentation creep behavior for amorphous selenium with varying temperature and strain rate has been found. A similarity contact analysis enables the extraction of the creep constitutive parameters and kinetic activation parameters, which provide insights into the mechanical instabilities in this rate-dependent solid. Such methods can be potentially generalized to other materials by means of high-temperature nanoindentation testing.

References

Argon, A.S., 1979. Plastic deformation in metallic glass. Acta Metall. **27**, 47-58.

Bower, A.F., Fleck, N.A., Needleman, A., Ogbonna, N., 1993. Indentation of a power law creeping solid. Proc. R. Soc. Lond. A **441**, 97-124.

Gao, Y.F., 2006. An implicit finite element method for simulating inhomogeneous deformation and shear bands of amorphous alloys based on the free-volume model. Modelling Simul. Mater. Sci. Eng. **14**, 1329-1345.

Gao, Y.F., Lucas, B.N., Hay, J.C., Oliver, W.C., Pharr, G.M., 2006. Nanoscale incipient asperity sliding and interface micro-slip assessed by the measurement of tangential contact stiffness. Scripta Mater. **55**, 653-656.

Gao, Y.F., Xu, H.T., Oliver, W.C., Pharr, G.M., 2008. Effective elastic modulus of film-on-substrate systems under normal and tangential contact. J. Mech. Phys. Solids **56**, 402-416.

Gao, Y.F., Yang, B., Nieh, T.G., 2007. Thermomechanical instability analysis of inhomogeneous deformation in amorphous alloys. Acta Mater. **55**, 2319-2327.

LaManna, J.A., 2006. Ph.D. Thesis, University of Tennessee, Knoxville, TN.

Li, H., Ngan, A.H.W., 2004. Size effects of nanoindentation creep. J. Mater. Res. **19**, 513-522.

Rice, J.R., 1977. Theoretical and Applied Mechanics, edited by Koiter, W.T., North-Holland, Amsterdam, 207-220.

Rudnicki, J.W., Rice, J.R., 1975. Conditions for the localization of deformation in pressure-sensitive dilatants materials. J. Mech. Phys. Solids **23**, 371-394.

Liu, F.X., Gao, Y.F., Liaw, P.K., 2008. Rate-dependent deformation behavior of Zr-based metallic-glass coatings examined by nanoindentation. Metall. Mater. Trans. A **39**, 1862-1867.

Lucas, B.N., Oliver, W.C., 1999. Indentation power-law creep of high-purity indium. Metall. Mater. Trans. A **30**, 601-610.

Mayo, M.J., Nix, W.D., 1988. A micro-indentation study of superplasticity in Pb, Sn, and Sn-38wt%Pb. Acta Metall. **36**, 2183-2192.

Needleman, A., 1988. Material rate dependence and mesh sensitivity in localization problems. Comput. Meth. Appl. Mech. Engng. **67**, 69-85.

Oliver, W.C., Pharr, G.M., 1992. An improved technique for determining hardness and elastic modulus using load and displacement sensing indentation experiments. J. Mater. Res. **7**, 1564-1583.

Pan, D., Inoue, A., Sakurai, T., Chen, M.W., 2008. Experimental characterization of shear transformation zones for plastic flow of bulk metallic glasses. Proc. Natl. Acad. Sci. **105**, 14769-14772.

Poisl, W.H., Oliver, W.C., Fabes, B.D., 1995. The relationship between indentation and uniaxial creep in amorphous selenium. J. Mater. Res. **10**, 2024-2032.

Spaepen, F., 1977. A microscopic mechanism for steady state inhomogeneous flow in metallic glasses. Acta Metall. **25**, 407-415.

Tang, B., Ngan, A.H.W., 2005. Investigation of viscoelastic properties of amorphous selenium near glass transition using depth-sensing indentation. Soft Mater. **2**, 125-144.

Wang, C.L., Zhang, M., Nieh, T.G., 2009. Nanoindentation creep of nanocrystalline nickel at elevated temperatures. J. Phys. D: Appl. Phys. **42**, 115405.

Yang, B., Wadsworth, J., Nieh, T.G., 2007. Thermal activation in Au-based bulk metallic glass characterized by high-temperature nanoindentation. Appl. Phys. Lett. **90**, 061911.

Appendix 1.1.
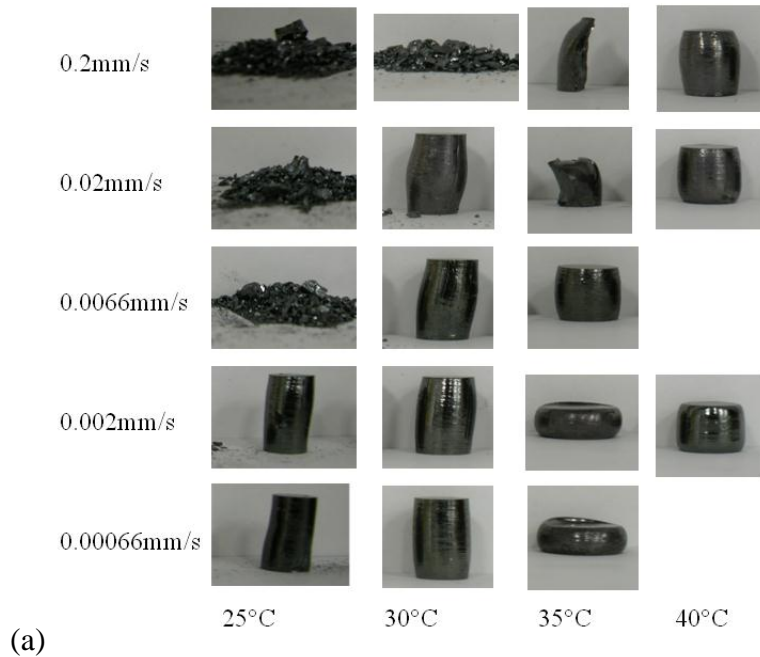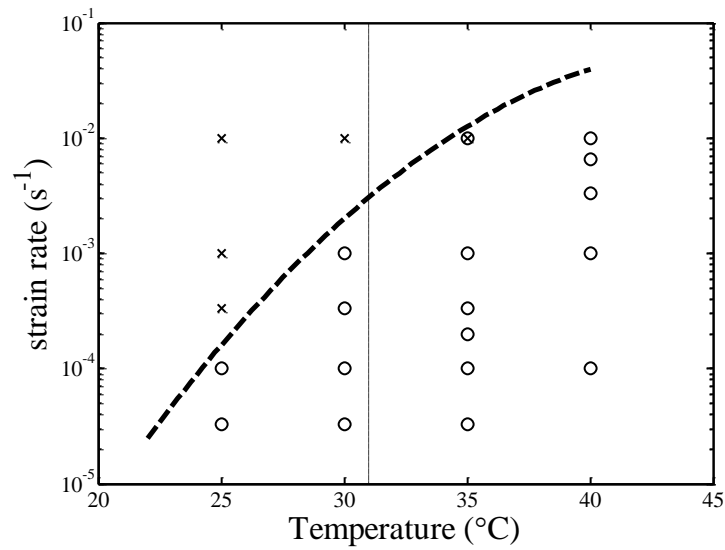
Figure 1.1. (a) Amorphous selenium samples after uniaxial compression exhibit homogeneous deformation (denoted as circles in (b)) or fragmentation (denoted as crosses in (b)); (b) The boundary that delineates these two deformation modes can be roughly illustrated by the thick dashed line on the temperature versus strain rate plot. Temperature varies from 25 ℃, 30 ℃, 35 ℃, to 40 ℃ from the top to the bottom row.
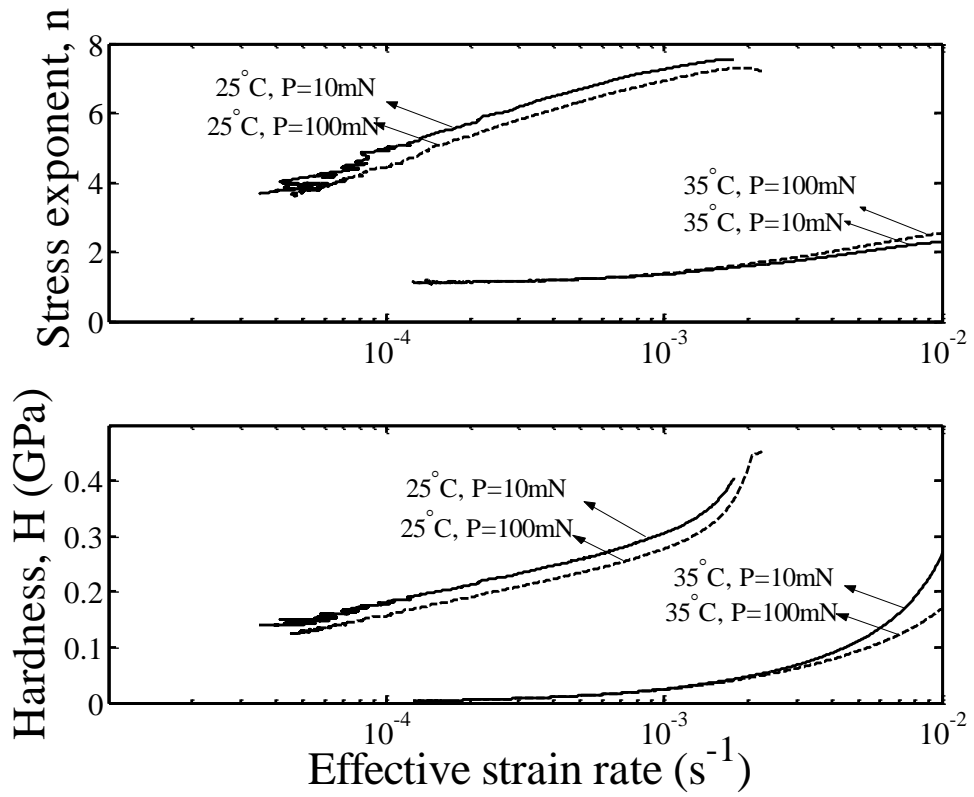
Figure 1.2. The variations of stress exponent, *n*, and nominal hardness, *H*, with respect to the applied load and temperature. Each line represents one load-and hold nanoindentation creep test.
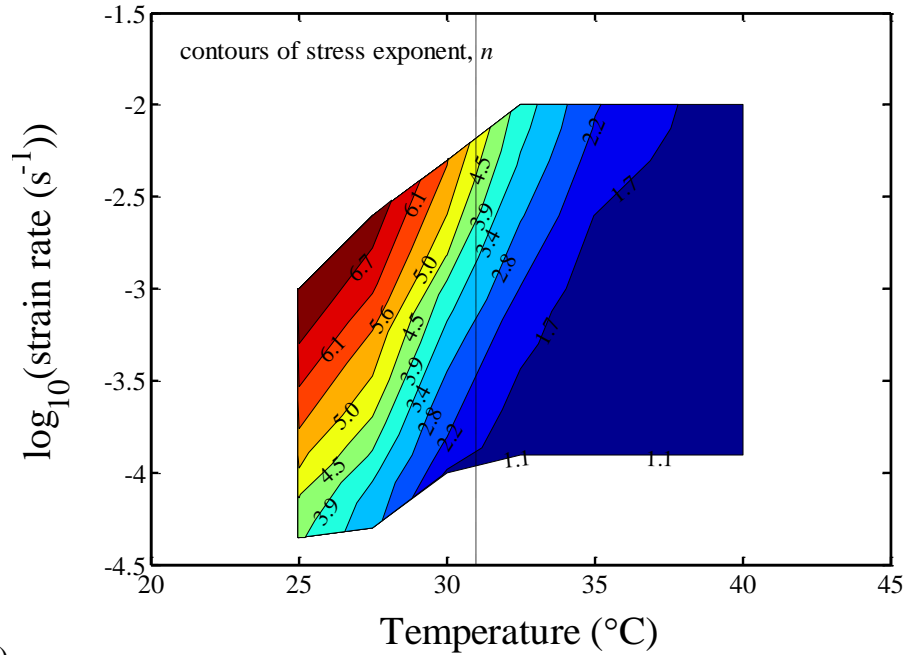
(a)
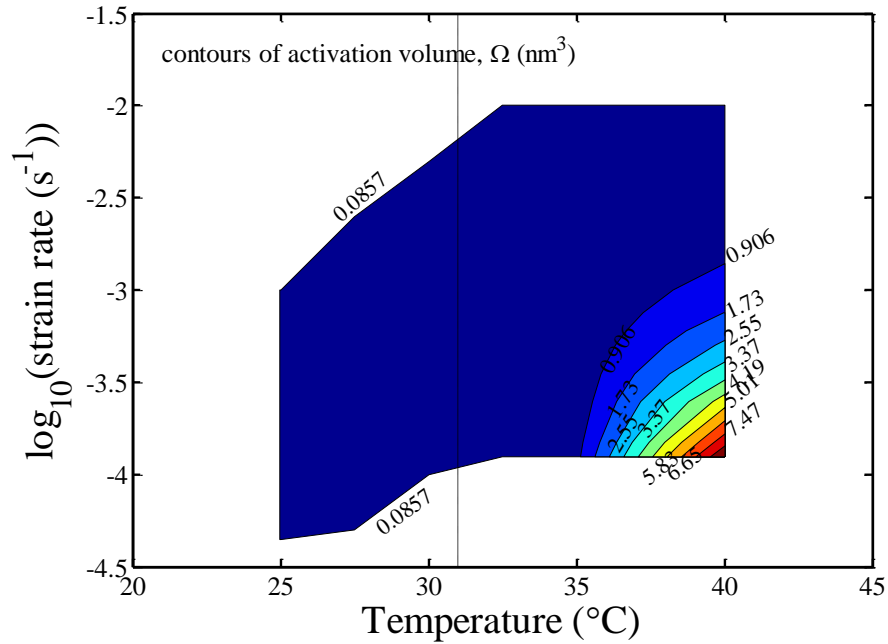
(b)

Figure 1.3. Contour plots of stress exponent, *n*, and activation volume, Ω, with varying temperatures versus strain rates. Data are obtained for the constant load-and-hold experiment with a constant load of 10mN.

CHAPTER II
Measurement of power-law creep parameters by instrumented indentation methods

A version of this chapter was submitted to *Journal of the Mechanics and Physics of Solids* on March 1st, 2012.

Authors:

C. J. Su, E. G. Herbert, S. J. Sohn, J. A. LaManna
Dept. of Materials Science and Engineering, University of Tennessee, Knoxville, TN 37996

W.C. Oliver
Nanomechanics Inc., Oak Ridge, TN 37830

G.M. Pharr
Dept. of Materials Science and Engineering, University of Tennessee, Knoxville, TN 37996; and Materials Science and Technology Division, Oak Ridge National Lab, Oak Ridge, TN 37831

C.J. Su's involvement in the article: prepared the samples, designed and performed indentation creep experiments, analyzed the experimental data, built theoretical models based on Bower's model, wrote and revised the article.

Co-researchers' contributions are listed as follows:

E.G. Herbert worked with Caijun to analyze the experimental data, prepare and revise the article.

S.J. Sohn improved Bower's model and performed finite element analysis.

J.A. LaManna performed uniaxial compression creep experiments.

W.C. Oliver provided technical support and worked with Caijun to analyze the experimental data.

 G.M. Pharr provided research guideline and worked with Caijun to analyze the experimental data, prepare and revise the article.

Abstract

New experimental methods are developed to measure the uniaxial power-law creep parameters α and n in the relation $\dot{\varepsilon} = \alpha\sigma^n$ ($\dot{\varepsilon}$ is the creep strain rate and σ is the creep stress) from indentation data obtained with a conical or pyramidal indenter. The methods are based on an analysis of Bower et al., which relates the indentation creep rate to the uniaxial creep parameters based on simple assumptions about the constitutive behavior (Bower et al., 1993). Using finite element simulations to establish the influences of finite deformation and transients caused by elasticity, the proposed methods are explored experimentally using amorphous selenium as a model material. This material is well suited for the study because it creeps at temperatures slightly above ambient in a load-history independent fashion with a stress exponent close to unity. Indentation creep tests were conducted with a Berkovich indenter using three different loading methods. With a few notable exceptions, the values of both α and n derived from the indentation data are generally in good agreement with those measured in uniaxial compression tests, thus demonstrating the validity of the approach.

1. Introduction

Instrumented indentation is widely used to investigate the mechanical properties of small volumes of material such as thin films, modified surfaces, individual phases, and microscopic devices (Asif and Pethica, 1997; Bucaille et al., 2002; Chu and Li, 1977; Grau et al., 1998; Li and Ngan, 2004; Lucas and Oliver, 1999; Lucas and Pendleton, 1982; Mayo and Nix, 1988; Oliver and Pharr, 1992; Poisl et al., 1995; Raman and Berriche, 1992; Su et al., 2010; Wang et al., 2010; Wang et al., 2009; Wilkinson and Ashby, 1975). Although indentation experiments are generally easy to perform, correctly interpreting the data can be challenging because of the complex nature of stress and strain during indentation contact. While this doesn't prevent meaningful evaluations of samples on a comparative basis, it is one of the primary obstacles to using indentation methods to evaluate the material constants that form the basis of design and modeling. To overcome this problem, theoretical modeling and numerical simulation techniques are frequently used to correlate the constitutive behavior of materials in uniaxial tension or compression to the load, displacement, and time data recorded during an instrumented indentation test (Atkins et al., 1966; Bower et al., 1993; Bucaille et al., 2002; Cheng, 2001; Fischer-Cripps, 2004; Hill, 1992; Lee et al., 2010; Mulhearn and Tabor, 1960; Ogbonna et al., 1995; Sargent and Ashby, 1992; Storakers and Larsson, 1994; Yang et al., 1995). However, these correlations are often limited in applicability based on the assumptions used in the models and simulations.

In this work, we explore the extent to which load and depth sensing indentation methods can be used to measure material creep parameters from simple measurements of indention load, P, depth, h, and time, t, and correlate them with them with creep parameters measured in uniaxial tension or compression. For uniaxial tests, steady state creep rates, $\dot{\varepsilon}$, are usually related to the uniaxial creep stress, σ, through the simple power law relation

$$\dot{\varepsilon} = \alpha \sigma^n \ , \tag{1}$$

where α and *n* are material parameters. From a simple dimensional standpoint, the stress in an indentation test should be related to the pressure exerted by the indenter, *p=P/A*, where *P* is the applied load and *A* is some appropriate measure of the area of the indentation contact (the exact definition of this area will be examined later). Moreover, for a geometrically self-similar indenter such as a cone or a pyramid, the indentation strain rate, $\dot{\varepsilon}_i$, should be directly related to $\dot{h}/h$, where $\dot{h}$ is the indentation displacement rate. This has led many investigators to suggest that for indentation creep there should be an expression equivalent to Eq. 1 of the form

$$\dot{\varepsilon}_i = \left(\frac{1}{h}\right)\left(\frac{dh}{dt}\right) = \beta p^N , \tag{2}$$

where β and *N* are material constants. In fact, it has been shown in numerous experiments that despite the remarkably different test geometries used for uniaxial and indentation creep testing, the exponents *n* and *N* are the same when steady state conditions are achieved, thus providing an experimental approach to determining the creep stress exponent from indentation data (Lucas and Oliver, 1999; Mayo and Nix, 1988; Raman and Berriche, 1992). However, the same is not true of the creep coefficients α and β , which are related in more complex ways due to the complex nature of the stresses and strains that develop during indentation. Thus, in order to *fully* characterize the uniaxial creep parameters in an instrumented indentation test, one must also be able to relate β to α .

Here, we examine such a relation developed by Bower et al. (Bower et al., 1993). Our experimental approach is to conduct uniaxial compression creep tests and indentation creep tests in a simple model material and use the results to explore several experimental methods that can conceivably be used to measure both α and *n* by instrumented indentation techniques. Since the methods follow directly from Bower et al's analysis, we begin by summarizing the relevant results of that analysis as they apply to the indentation conditions we have used to make the measurements. We also present finite element simulations that help to provide insight about when the analysis can be safely applied. The methods are tested by using them to analyze indentation creep in amorphous

selenium, a material that creeps in a well defined way at temperatures slightly above ambient.

2. Bower's analysis

The analysis developed by Bower et al., hereafter referred to as the Bower's analysis or Bower's method, is based on the contact geometry shown in Fig. 2.1. As originally developed, the analysis applies to a number of indenter geometries, but for simplicity, we limit its application here to a conical indenter since the cone mostly closely approximates the geometrically self-similar form of the Berkovich indenter - a triangular pyramid - used in experiments. As shown in the figure, at any time, t, the conical indenter, which has a half-included angle, θ, creeps into the material at a load, P, to a depth, h, where the reference for the depth is the initially undeformed surface. The indenter velocity, v, at any time is given by $v = dh/dt$. Since material can pile-up or sink-in during deformation, the depth along which contact is made, h_c, will in general be different from the nominal measured depth, h. In a similar manner, the true contact radius, a_c, will be different from the nominal contact radius, a_{nom}, and the true mean contact pressure, $p_m = P/\pi a_c^2$, will differ from the nominal contact pressure, $p_{nom} = P/\pi a_{nom}^2$. The nominal parameters are especially convenient because they can be deduced directly from the measured indenter displacement, h, and the indenter geometry since $\tan\theta = a_{nom}/h = a_c/h_c$. For this reason, we focus on the ways in which Bower's analysis can be applied to the nominal contact parameters.

Bower's model and analysis assume a pure power-law creeping material in which elastic deformation is ignored and the material is assumed to be history independent. The latter implies that the instantaneous strain rate is determined only by the instantaneous value of the mean contact pressure and is not influenced by previous deformation or straining. This assumption would apply, for instance, to a material that always creeps in the steady state, but not to one in which significant creep transients follow a load or stress change. An important consequence of this assumption is that the strain rate and stress

29

fields are identical to those under a rigid flat punch of radius a indenting a creeping half-space at a velocity of dh/dt, which provides a means to solve the problem by non-linear elastic finite element calculations.

As illustrated in Fig. 2.1, Bower's analysis also pays special attention to the amount of pile-up or sink-in around the contact, since this can have significant affects on the true contact area and, thus, the true contact stresses. The degree of pile-up or sink-in is measured through a pile-up/sink-in parameter, c, given by

$$c = a_c / a_{nom} = h_c / h = \sqrt{A_c / A_{nom}} \, , \tag{3}$$

where A_c is the true projected contact area and A_{nom} is the nominal projected area. Note that although A_c is the more physically meaningful parameter, A_{nom} is experimentally more convenient because it can be determined directly from the indenter geometry and the measured depth of penetration. Note also that being able to relate c to the indentation areas provides a convenient way to account for pile-up and sink-in when the contact is non-circular, as is the case for the Berkovich indenter used in the experiments.

The primary prediction of Bower's analysis is a relation between the indentation strain rate and the mean contact pressure, which for a conical indenter reduces to:

$$\dot{\varepsilon}_i = \left(\frac{1}{h} \right) \left(\frac{dh}{dt} \right) = \frac{\alpha \tan \theta}{F^n c^{2n-1}} \left(p_{nom} \right)^n \, . \tag{4}$$

Here, F is an important non-dimensional parameter referred to as the *"reduced contact pressure"* which is determined from non-linear elastic finite element simulations. Bower's analysis shows that both F and c are functions of the stress exponent, n, with a significant portion of his analysis aimed at establishing these relationships. Note that if we let the indentation contact pressure, p, in Eq. 2 be the nominal contact pressure, p_{nom}, then Eq. 4 is exactly of the form of Eq. 2 with $N = n$, thus providing a theoretical underpinning for use of Eq. 2 with $N = n$. Comparison of Eq. 4 with Eq. 2 also reveals that

$$\beta = \frac{\alpha \tan \theta}{F^n c^{2n-1}} \quad or \quad \alpha = \frac{\beta F^n c^{2n-1}}{\tan \theta} \, , \tag{5}$$

thereby providing the relation needed to determine the value of the uniaxial creep coefficient α from indentation measurements of the parameter β. We have

intentionally written Eq. 4 in terms of p_{nom} rather than p_m to make it useful from an experimental perspective.

To complete the analysis, Bower et al. used non-linear elastic finite element analyses for a cylindrical flat punch indenter to determine the dependencies of c and F on n. The flat punch analysis, as opposed to one for a specific indenter geometry, is justified given that the basic constitutive law for a pure creeping solid is one for which the deformation behavior at any instant is history independent and depends only on the instantaneous velocity and radius of contact. However, the flat punch finite element calculations ignore finite deformation effects, which are moderately important for conical indenters, giving values for c and F that depend on the indenter angle θ as well as n. Thus, in this work we have also performed full field finite element simulations for an elastic-power-law-creeping solid to establish the dependencies of c and F on n and θ. In addition, we have used these simulations to establish the importance of elasticity on the deformation process, an effect that is observed in the experiments presented here but not included in the Bower's analysis. Elasticity produces an initial transient in the displacement-time behavior as the contact geometry changes from entirely elastic just after application of the load to one in which contact geometry and stress distribution settle in to those of a pure creeping solid. These transients can be quite lengthy, depending on deformation conditions, so some knowledge of their duration is needed to properly analyze experimental data.

3. Application to instrumented indentation testing

Instrumented indentation creep tests are most often performed with load-time histories that utilize either a constant load and hold (CLH) or a constant rate of loading (CRL) (Mayo and Nix, 1988; Raman and Berriche, 1992). As the name implies, the CLH method maintains a constant, prescribed load P on the indenter, while in the CRL method, the loading rate, $\dot{P} = dP/dt$, is maintained constant. In both cases, the indenter displacement, h, is measured as a function of time, t. Another method of significant

31

practical interest, but less frequently employed because it is more difficult to implement, is the constant strain rate (CSR) method (Lucas and Oliver, 1999). The CSR technique involves loading a geometrically self-similar indenter (cone or pyramid) in such a way that the loading rate divided by the load, $\dot{P}/P$, is held constant. For a material whose hardness is constant with depth, i.e., a bulk, homogeneous solid exhibiting no indentation size effect, the constant $\dot{P}/P$ produces a constant strain rate that is proportional to the indentation strain rate, $\dot{h}/h$. Accordingly, each CSR experiment generates a single data point on a plot of strain rate versus mean pressure or stress. All three methods are employed experimentally in this work.

Before proceeding, it is useful to examine the displacement-time behavior (*h-t*) expected from the CLH and CRL methods based on the results of Bower's analysis, since the *h-t* relations can be used directly to determine basic uniaxial creep parameters from experimental indentation data. For the constant load method (CLH), integration of Eq. 4 yields:

$$h = (2n\beta)^{1/2n} \left(\frac{P}{\pi \tan^2 \theta} \right)^{1/2} t^{1/2n} \quad , \tag{6}$$

which shows that the creep exponent *n* can be evaluated directly from the slope of a log-log plot of *h vs. t*, and that once *n* is known, the indentation creep coefficient β can be similarly extracted from the data. For the constant loading rate method (CRL), integration of Eq. 4 yields:

$$h = \left(\frac{2n\beta}{n+1} \right)^{1/2n} \left(\frac{\dot{P}}{\pi \tan^2 \theta} \right)^{1/2} t^{(n+1)/2n} \quad , \tag{7}$$

so once again, evaluation of the material constants β and *n* is facilitated through a log-log plot of *h vs. t*. For the CRL method, data analyses are also facilitated through an examination of the force-displacement relation (*P-h*), which is given by:

$$P = \left(\frac{n+1}{2n} \frac{\dot{P}}{\beta} \right)^{1/(n+1)} \left(\pi \tan^2 \theta \right)^{n/(n+1)} h^{2n/(n+1)} \quad . \tag{8}$$

Note that none of these relations accounts for elastic displacements, a point we will revisit later.

4. Finite element analysis

4.1 Simulation procedures

Full-field finite element simulations were used to model the indentation of an elastic-power-law-creeping solid using the ABAQUS™ finite element software version 6.3-5. The objectives of the simulations were: (1) to evaluate the dependence of the material parameters c and F on n and θ in a manner that accounts for finite deformation; and (2) to evaluate the extent of the initial transients in the h-t behavior caused by elastic deformation. The simulations were performed using the finite-strain/finite-deformation feature of ABAQUS™, using an elastic-viscoplastic constitutive relation that models rate-dependent, isotropic deformation using the Mises flow criteria. The uniaxial constitutive relationship for the elastic-power-law creeping solid was defined by

$$\dot{\varepsilon} = \left(\frac{\dot{\sigma}}{E}\right) + \alpha\sigma^n \ , \tag{9}$$

where E is Young's modulus. Poisson's ratio, v, was fixed at 0.3, and the creep exponent, n, was varied from 1 to 10. The simulations were conducted for three half-included cone angles - 60°, 70°, and 80° - which span the range of the Berkovich indenter used in experiment. Based on equal projected cross-sectional areas, the equivalent cone angle for a Berkovich indenter is 70.3°. The indenter was modeled as rigid, and the creeping solid as a cylinder with a free boundary at the outside and roller boundary conditions at the bottom. A semi-infinite half-space condition was achieved by assuring that the radius and length of the cylinder exceeded the maximum contact radius by a factor of at least 100.

A mesh employing 4593 linear, fully-integrated elements was used to model the cylinder, with a fine mesh of smaller elements employed close to the indenter tip region to accurately determine the contact radius and the pile-up/sink-in geometry. The maximum contact radius was always kept within the boundary of the fine mesh zone to avoid mesh transitioning effects. The indentation depth, h, and contact radius, a_c, were

recorded each time the indenter encountered a new surface node. Average values of load, depth, contact radius, and time at successive nodes were used to calculate the mean pressure and strain rate.

Finite element simulations were performed for both the constant load and hold method (CLH) and the constant rate of loading method (CRL). Under CLH conditions, a constant load was prescribed on the indenter and the resulting depth and contact radius were monitored as a function of time. Under CRL conditions, the load was linearly increased with time while the resulting depth and contact radius were recorded. Dimensional analysis was used to non-dimensionalize the problem and limit the number of simulations needed to explore the desired parameter space (Potter and Wiggert, 1991).

4.2   Evaluation of uniaxial material creep parameters from indentation data

As an integral part of evaluating the uniaxial creep parameters from indentation data by means of Bower's analysis, one must know how the pile-up/sink-in parameter, c, and the reduced contact pressure, F, depend on the stress exponent, n, and indenter angle, θ, for finite deformation conditions. Determination of these dependencies for c from finite element observations was relatively straightforward since $c = a_c/a_{nom} = h_c/h$ (see Fig. 2.1). Thus, c was evaluated simply by measuring a_c from the geometry of the finite element contact profiles.

Figure 2(a) shows the dependencies of c on n for three different indenter angles based on CRL simulations at times and indentation depths well beyond the elastic transient (note: how the length of the elastic transient was evaluated is addressed later). For comparison, Bower's flat punch finite element results are also shown. Although the new results tend to Bower's as the cone angle approaches $90°$, it is clear that the non-$90°$ angles produce small, but distinct deviations from Bower's results that could have an influence on the accuracy of measurements. The lines through the data points are regressions of the form:

$$c(n, \theta) = \frac{h_c}{h} = c_0 + c_1\left(\frac{1}{n}\right) + c_2\left(\frac{1}{n}\right)^2 + c_3\left(\frac{1}{n}\right)^3 , \tag{10}$$

34

where the best fit parameters are given in Table 2.1.

Finite element evaluation of the reduced contact pressure, F, follows from its relation to the creep coefficients α and β in Eq. 5. To do this, load-displacement data (P-h) from CRL simulations after the elastic transient had dissipated were first used to determine the indentation creep coefficient β by means of Eq. 8. Then, using the values of α and n used as input in the finite element simulations and the known load and indenter angle, F was computed directly from Eq. 5.

The dependence of F on n and θ is shown and compared to Bower's results in Fig. 2.2(b). Like the pile-up/sink-in parameter, c, the large deformation simulation results tend towards Bower's prediction as the cone angle approaches 90°, but exhibit potentially important differences for smaller cone angles, especially for larger values of n. Note that all three cone angles show a peak in F when $1/n$ is small ($< \sim 0.15$), as was also observed by Bower. The relations between F and $1/n$ are well described by a fourth order polynomial of the form:

$$F(n,\theta) = F_0 + F_1\left(\frac{1}{n}\right) + F_2\left(\frac{1}{n}\right)^2 + F_3\left(\frac{1}{n}\right)^3 + F_4\left(\frac{1}{n}\right)^4 ,$$
(11)

where the fit parameters are given in Table 2.2.

4.3 Elastic transients

As previously discussed, elastic deformation in the early stages of creep can contribute significantly to the measured displacement and, therefore, produce significant deviations from the long term creep behavior that are observed as transients in the h-t behavior at the beginning of a test. To identify when the elastic transient is important and when it can be safely ignored, finite element simulations for constant load and hold experiments (CLH) were conducted to generate displacement-time data sets which included the transient. To identify the extent of the transient, the finite element h-t data sets were analyzed point by point along the creep curve to extract the indentation creep parameters n and β by local fits of the h-t data to Eq. 6 using 10 consecutive data points.

The uniaxial creep coefficient, α_{out}, was then evaluated from using the locally determined n and β by means of Eq. 5 for comparison to the true value input into the simulations, α_{in}. If there were no transient, these ratios should be precisely one.

Results are shown in Fig. 2.3, where the ratios of the output to input n stress exponents (n_{out}/n_{in}) and output to input uniaxial creep coefficients (α_{out}/α_{in}) are plotted as a function of the non-dimensional indenter displacement, $h/h_{elastic}$. The elastic displacement, $h_{elastic}$, which for a conical indenter is given by

$$h_{elastic} = \sqrt{\frac{\pi P}{2E^* \tan\theta}} \ , \tag{12}$$

where $E^* = E/(1-v^2)$, was found to be a convenient non-dimesionalizing parameter that elimnates the dependence of the observed behavior on the applied load, P (Sneddon, 1965). This follows from the non-dimensionalized form of Eq. 6, which can be written as:

$$\frac{h}{h_{elastic}} = (2n\beta)^{1/2n}\left(\frac{2E^*}{\pi^2 \tan\theta}\right)^{1/2} t^{1/2n} \ . \tag{13a}$$

For a constant rate of loading experiment (CRL), the equivalent normalization is:

$$\frac{h}{h_{elastic}} = (n+1)^{-1/2n}(2n\beta)^{1/2n}\left(\frac{2E^*}{\pi^2 \tan\theta}\right)^{1/2} t^{1/2n} \ . \tag{13b}$$

Figure 3a shows that due to the elastic influences, the value of n predicted from the simulated CLH data is within 2% of the input value only when the total measured displacement is 10 times greater than the elastic displacement. Fig. 2.3(b) shows that the predicted creep coefficient, α, is much more sensitive to the effect of elasticity, particulalry as n gets large. When $h/h_{elastic}=10$, α_{out} is overestimated by about 25% when $n = 5$, but only 3 to 4% when $n = 1$. Quantitatively similar results were obtained in the CRL simulations. These results lead to three important conclusions: 1) elasticity can indeed cause significant deviations from the thoretical h-t relationships and, therefore, generate important errors in the derived values of α and n; 2) the error in α depends on n, whereas the error in n is virtually independent of n; and 3) the error in n due to the

effect of elasticity is generally negligible when $h/h_{elastic}$ is greater than 10, but the error in α may still be important.

From a practical perspective, it is useful to note that the criteria $h/h_{elastic}>10$, for which the stress exponents derived from the proposed method of analysis are close to correct, corresponds to absolute indentation depths of

$$h > 10\sqrt{\frac{\pi P}{2E^* \tan \theta}} \ , \tag{14}$$

and nominal or mean indentation pressures of

$$p_{nom} < \frac{E^*}{50 \pi^2 \tan \theta} \ \text{or} \ p_m < \frac{E^*}{50 \pi^2 c^2 \tan \theta} \ . \tag{15}$$

Thus, if the elastic modulus of the creeping material is known, these relations could provide experimental guidance on how to obtain results that are uninfluenced by the elastic transient.

5.   Experimental assessment

The validity of the proposed methods for evaluating α and n from instrumented indentation data were assessed by conducting experiments in amorphous selenium. This material has a glass transition temperature, T_g, of 31.0 ± 0.5 ℃, and creeps in very well defined way at slightly higher temperatures (e.g., 35 ℃) (Poisl et al., 1995). Thus, simple modifications of commercially available indentation and uniaxial tension/compression systems could be used to characterize the creep behavior without the complications of conducting very high temperature tests. The samples were prepared by melting pure amorphous selenium shot (Alfa Aesar®) and quenching it into chilled copper molds. Specific details of the sample processing technique have been described elsewhere (Su et al., 2010). The amorphous microstructure was confirmed by x-ray diffraction.

Compression testing was used to establish the uniaxial creep parameters. The compression tests were performed on cylindrical specimens nominally 1 cm in diameter and 2 cm in length using an MTS 10/GL screw driven uniaxial tension/compression load

frame equipped with an environmental chamber. A 250 W heat lamp and two air circulation fans placed inside the environmental chamber provided uniform heating. The temperature in the chamber was controlled from 25.0 ℃ to 35.0 ℃ with 0.01 ℃ precision by a proportional temperature controller that regulated the amount of power supplied to the heat lamp based on feedback from a precision platinum thermometer. Compression tests were conducted at temperatures of 25.0 ℃, 30.0 ℃, and 35.0 ℃. The samples were compressed not a constant load but rather at constant displacement rates of 0.66, 2, 6.6, 20, or 200 μm/s. Thus, the tests were not true creep tests, but at the higher temperatures a constant flow stress (not varying with strain) was sometimes achieved after an initial transient, thus indicating that steady state flow conditions were reached. Under these circumstances, constant strain rate tests are equivalent to constant load creep tests, and meaningful steady state creep parameters can be extracted from the data. The compression tests were terminated either at 50% strain or when the material failed.

Indentation creep experiments were performed at 25.0 ℃, 30.0 ℃, and 35.0 ℃ using an MTS Nano Indenter XP equipped with a Berkovich diamond indenter. As in the compression tests, the system was heated by placing a 250 W heat lamp inside the environmental isolation cabinet and gently stirring the air with two small computer fans. The fans and lamp were placed on the floor directly beneath the vibration table, using the same precision temperature controller and platinum resistance thermometer used in the compression experiments. Within 24 to 36 hours, the forced-convection heating system brought the entire instrument to thermal equilibrium to within ± 0.01 ℃. The sample was placed in the cabinet one hour before tests to avoid long term exposure that could lead to crystallization, which can be identified by a change in the surface appearance from mirror like to dull gray luster. The thermal drift rate for starting a test was prescribed at 0.05 nm/s.

Three types of indentation creep experiments were performed: (1) constant load and hold (CLH), (2) constant loading rate (CLR), and (3) constant strain rate (CSR). For the CLH experiments, the specimen was loaded to the target load of 1, 10, 100, or 500 mN in 2 seconds and then held constant for period of 1 hour or until the displacement reached 50 μm, whichever occurred first. As the sample crept, the applied load was

continuously adjusted to compensate for the displacement of the indenter support springs, thereby ensuring the load on the sample was held constant during the entire hold period. The CRL experiments were performed at constant loading rates of 1, 10, 100, 1,000, and 10,000 µN/s and were terminated when either the depth reached 50 µm, the load reached the instrument limit of approximately 600 mN, or the time exceeded 10,000 s, whichever criteria was met first. The CSR experiments were performed at constant $\dot{P}/P$ = 0.1, 0.01, 0.001, and 0.0001 s^{-1}. As in the CRL experiments, the CSR tests were terminated at either a depth limit of 50 µm, a load limit of 600 mN, or a time limit of 10,000 s. For each of the three test methods, the measurements were repeated four times.

After indentation testing, the specimens were quickly removed from the heated chamber and cooled on a brass block stored in a refrigerator at approximately 4 ℃. This was done to preserve the contact geometry of the final indentation for 3D imaging of the hardness impressions using an ADE Phase Shift MicroXAM^{TM} surface mapping microscope. The resulting 3D contour images were used to measure of the true projected area of the contact and quantify the amount of pile-up or sink-in. Although the lateral resolution of the technique is limited by the wavelength of light (approximately 1 µm), the hardness impressions were large enough, typically 83 µm across, that accurate measurements could be obtained.

6.   Results and discussion

6.1   Uniaxial compression testing

Figure 4 shows the true stress - true plastic strain curves for amorphous selenium tested in compression at 25 ℃, 30 ℃, and 35 ℃. True stress and true strain were calculated based on the assumption of conservation of volume. The plastic strain was determined by subtracting the elastic strain computed from the slope of the initial linear portion of the data from the total strain. The tests were found to be very repeatable, so for the sake of clarity, only data from one of the four experiments at each displacement rate are included in the figure.

The data for the 35 ℃ tests are shown in Fig. 2.4c. The tests at the three slower strain rates all exhibit a relatively constant flow stress after an initial transient period, indicating that a true steady state was achieved and that the steady state flow stresses can be used to represent those in constant stress creep tests. On the other hand, in the tests conducted at the fastest strain rate, 0.2 mm/s, and to a lesser degree the second fastest, 0.02 mm/s, there is a distinct maximum in the flow stress followed by strain softening. As reported by Su et al., the high strain rate behavior is associated with a transition from uniform plastic deformation along the gauge length to inhomogeneous deformation in which the strain is localized into shear bands (Su et al., 2010). For this reason, the 35 ℃ data at the two highest strain rates may not be representative of true steady state creep and thus of questionable value in the analysis.

As shown in Figs. 4a and b, the data obtained at 25 ℃ and 30 ℃ exhibited the flow stress peak and non-steady behavior at all strain rates, with the specimens tested at the highest rates (0.2 mm/s) exploding into fragments after little or no plasticity. Thus, unfortunately, none of the 25 ℃ and 30 ℃ data are appropriate for a steady state creep analysis.

Figure 5 shows the strain rates for the data in Fig. 2.4 plotted as a function of the stress at 2% plastic strain. The filled symbols represent tests in which steady state conditions were fully achieved. The three lowest strain rate data points at 35 ℃, which are known to be steady state, give $n = 1.15$ and $\alpha = 1.04 \times 10^{-12}$ $Pa^{-1.15}s^{-1}$. Also shown for comparison are the data of Stephens, who measured the shear viscosity, η, of amorphous selenium at 35 ℃ in tensile creep tests, assuming $n = 1$ (Stephens, 1978). We have converted his measured values of the viscosity for comparison to our compression data using the relation

$$\eta = \frac{\sigma}{3\dot{\varepsilon}} = \frac{1}{3\alpha} \quad , \tag{16}$$

which gives $\alpha = 1.20 \times 10^{-11}$ $(Pa\ s)^{-1}$. The dashed line in Fig. 2.5 shows that Stephens' measurements are very similar to those obtained here for the steady state data.

For completeness, the data at 25 ℃ and 30 ℃ are also included in the figure, using the stress at 2% plastic strain, which is usually close to the peak stress, as the

representative stress value. However, because these data are probably not representative of steady state creep, they are not generally considered further in our analyses.

6.2   Indentation testing - constant load and hold method (CLH)

Figure 6a shows the indentation h - t curves at four load levels in the range 1 to 500 mN for CLH indentation creep experiments performed at 35 ℃. For each load, 4 separate data sets are included, but because the data are so reproducible it appears that there is only one curve at each load. Figure 6b shows the same data re-plotted to normalize the creep displacements with respect to the elastic displacement, $h_{elastic}$, computed from Eq. 12 and assuming $E^* = 10.3$ GPa. This value of E^* is derived from the 35 ℃ elastic property measurements of Vedam et al. and Etienne et al., who found a shear modulus G of 3.5 GPa and a Poisson's ratio v of 0.32 GPa, giving $E = 9.2$ GPa and $E^* = 10.3$ GPa (Etienne et al., 1979; Vedam et al., 1966). In Fig. 2.6b, the creep data in Fig. 2.6a clearly collapse onto a single curve independent of the applied load, as is predicted by Eq. 13a. This suggests that even though the creep behavior may exhibit an elastic transient and may not deform by pure power law creep alone until longer times and larger strains, the material still behaves in a manner consistent with the Bower's assumption that the deformation behavior is loading-history independent.

In Fig. 2.7, we have re-plotted the data in Fig. 2.6 as the indentation strain rate, $\dot{h}/h$, vs. the nominal mean pressure, p_{nom}, on log-log axes. Since p_{nom} can be computed directly from the measured indentation depth without a knowledge of the amount of pile-up or sink-in, this representation of the data is possible from measured parameters without any assumptions about the material behavior. Although the nominal mean pressure and the true mean pressure could deviate significantly if the amount of pile-up or sink-in were large, the indentation creep exponent extracted from such data, once the transient dissipates, should be unaffected since the true mean pressure and the nominal mean pressure for the self-similar indenter would differ only by only a multiplicative constant. As expected based on the load-history independence, the data in Fig. 2.7 do indeed all fall on a single curve, and it is linear over a large range on the log-log plot. The

slight deviation from linearity at the upper right, which is data from the initial portion of the test at small times and strains, indicates a small initial transient at nominal mean pressures greater than 0.1 GPa. Analysis of the linear portion of the data for $h > 10h_{elastic}$ according to Eqs. 4 and 5 yields $n = 1.12$, $\beta = 5.88$ x 10^{-12} Pa$^{-1.12}$s^{-1}, and $\alpha = 1.53$ x 10^{-12} Pa$^{-1.12}$s^{-1}, which compare favorably to the values measured in uniaxial compression, $n = 1.15$ and $\alpha = 1.04$ x 10^{-12} Pa$^{-1.15}$s^{-1}. It is important to note that the exact value of α deduced from the data in Fig. 2.7 depends on the assumed value of n. If we use $n = 1.15$ rather than $n = 1.12$, then α is 1.03 x 10^{-12} Pa$^{-1.15}$s^{-1}, which is in even closer agreement with the uniaxial compression data. These observations suggest that Bower's analysis can indeed be used to extract uniaxial creep parameters from indentation data with relatively good accuracy.

Another check on the applicability of the Bower's analysis follows from measurement of the pile-up/sink-in parameter, c. Figure 8 is an optical micrograph of an indentation made at 35 ℃ using the CLH method at a load of 10 mN obtained using the interferometric surface mapping microscope. The micrograph shows that material is significantly sunk-in all the way around the contact perimeter, including the corners of the indentation. Based on measurements of the ratio of the actual contact area in the micrograph to the nominal contact area determined from the depth of penetration and the indenter geometry, Eq. 3 yields $c = \sqrt{A_c/A_{nom}} = 0.69$. This compares favorably to the value $c = 0.71$ obtained from the $\theta = 70°$ finite element simulations using Eq. 10 and $n = 1.12$. Thus, the Bower's analysis also correctly predicts the pile-up / sink-in behavior, at least under these creep conditions. In the analyses that follow, we will assume that $c = 0.71$ is the correct value.

As discussed previously, an alternative method for measuring creep parameters from experimental data obtained in constant load and hold tests follows from the predicted form of the h-t curve given by Eq. 6. To explore this and examine the effects of the elastic transient on the analysis procedures, we reconsider the 35 ℃ CLH data in Fig. 2.6. Pertinent results are shown in Fig. 2.9 where, like the analysis of the finite element data in Fig. 2.3, the stress exponent and creep coefficient have been derived from the h-t

42

data by a point-to-point analysis according to the form of Eq. 6. As shown in Fig. 2.9a, the stress exponent derived from the analysis starts from a value close to 2 at short times but decreases asymptotically toward the value $n = 1.12$ at longer times. As shown in Fig. 2.9b, it is evident that n becomes constant at a normalized displacement $h/h_{elastic}$ of about 10, in agreement with the finite element simulations. Thus, a transient is indeed observed in the behavior that has features consistent with a transition from elastically dominated to power-law creep dominated behavior. However, a close comparison of the experimental data in Fig. 2.9 with the finite element predictions in Fig. 2.3a reveals that although the trends in the two data sets are qualitatively the same, the absolute magnitudes are not. Specifically, at a particular value of $h/h_{elastic}$ in the range $h/h_{elastic}<10$, the experimental stress exponents are measurably larger than those in the finite element simulations. This could be an indication that when the indentation stresses are high during the initial stages of the constant load experiment, the effective stress exponent may in fact be larger than 1.12, as might be expected if the material were to exhibit power law breakdown at high stresses like that observed in metals. This suggests that the transient may in fact have two separate origins - one from elasticity and another from a more complex uniaxial constitutive relation than cannot be described by a simple power law with a unique stress exponent. Equivalent point-to-point evaluation of α is complicated by the fact that the value and units of α depend on the local value of n. Thus, a similar plot of α vs. time or indenter displacement is not particularly meaningful. On the other hand, once the transient diminishes, the value of α remains relatively constant at a value that is useful for comparison. The average value at the end of the curves in Fig. 2.9 assuming $n = 1.12$ is $\alpha = 1.51 \times 10^{-12}$ Pa$^{-1.12}$s^{-1}, which within reasonable error is essentially the same with the value obtained from the data in Fig. 2.7, $\alpha = 1.53 \times 10^{-12}$ Pa$^{-1.12}$s^{-1}.

6.3   Indentation testing - constant rate of loading method (CRL)

Figure 10a shows the indentation $h - t$ curves for the tests conducted at 35 ℃ at a constant rate of loading, $\dot{P}$. In all, five different rates varying over 5 orders of magnitude

were examined: $\dot{P}$ = 1, 10, 100, 1000, and 10,000 µN/s. As in the case of the constant load and hold tests (CLH), it is useful to normalize the displacement by the elastic displacement, $h_{elastic}$. However, the elastic displacement for a CRL test is not a single value but rather varies with time because the load continuously increases during the test. Therefore, the elastic displacement must be computed from:

$$h_{elastic} = \sqrt{\frac{\pi \dot{P} t}{2 E^* \tan \theta}} \quad . \tag{17}$$

Data normalized in this way are shown in Fig. 2.10b where it is seen that the normalization does indeed bring the data toward a single master curve, thus once again confirming that the deformation behavior is largely load-history independent, at least at longer times and larger displacements. However, the inset in Fig. 2.10b shows that there is a measurable deviation from master curve behavior at the beginning of the test. The importance of this is seen in Fig. 2.11, where the h-t data have been re-plotted as the indentation strain rate vs. the nominal mean pressure. For nominal mean pressures less than 0.1 GPa, data from all five of the loading rates converge to a single curve, which, when analyzed according to Eqs. 4 and 5 give n = 1.12, β = 6.23 x 10^{-12} $Pa^{-1.12}s^{-1}$, and α = 1.62 x 10^{-12} $Pa^{-1.12}s^{-1}$. These parameters are very similar to those measured in the CLH tests. On the other hand, for p_{nom}>0.1 GPa, there is a clear separation of the curves (see inset in Fig. 2.10b), with higher loading rates producing much higher indentation strain rates. Thus, the creep behavior at short times is load-history dependent and inconsistent with Bower's analysis assumptions.

To further illustrate this, the stress exponents derived from a point-to-point analysis of the h-t data according to the form of Eq. 7 are shown in Fig. 2.12. The plots show that n tends toward a constant value of 1.12 at long times (Fig. 2.12a) and large penetration depths (Fig. 2.12b), but that very different, loading-rate-dependent values are obtained at small depths. Once again, the relatively constant values are obtained when $h/h_{elastic}$>10.

It is also of interest to note that the mathematical forms of Eqs. 13a and 13b suggest that there is a natural way to directly compare h-t data obtained in CRL and CLH

44

tests, provided the behavior is largely history independent, as seems to be the case at all but the shortest times in the CRL tests. Specifically, if Eq. 13b is rewritten as:

$$\frac{h}{(n+1)^{-1/2n} h_{elastic}} = (2n\beta)^{1/2n} \left(\frac{2E^*}{\pi^2 \tan\theta} \right)^{1/2} t^{1/2n} \quad , \tag{13c}$$

then its right hand side is exactly the same as Eq. 13a. Thus, CRL and CLH h-t data should be same way if the CLH displacements are normalized as $h/h_{elastic}$ and the CRL displacements as $h/[(n+1)^{-1/2n} h_{elastic}]$. Assuming $n = 1.12$, data normalized in such a way from a 10 mN CLH test and a 10 mN/s CRL test are compared in Fig. 2.13, where the strong coincidence is apparent.

6.4   Indentation testing - constant strain rate method (CSR)

Basic experimental results from constant strain rate tests (CSR), which were conducted at $\dot{P}/P = 0.1$, 0.01, 0.001, and 0.0001 s^{-1}, are given in Fig. 2.14. Figure 14a shows how the indentation strain rate varies with indenter displacement and Fig. 2.14b the same for the nominal mean pressure. The values of $\dot{h}/h$ and p_{nom} displayed on the plots are those at the end of the test. The curves show that there is indeed a tendency for $\dot{h}/h$ and p_{nom} to approach steady values, as is expected for the constant strain rate method (Lucas and Oliver, 1999). For the slowest strain rate, $\dot{P}/P = 0.0001$ s^{-1}, it appears that the test was terminated due to a time maximum before the true steady values were achieved. One curious feature in the plots is that for the tests conducted at higher rates, the steady values are approached from below whereas at slower rates, the steady values are approached from above. This is most likely not a real material effect, but rather a testing artifact caused by inadequate feedback control at short times for the higher rates.

The relation between the final indentation strain rates and the nominal mean pressures is shown in Fig. 2.15. Included for comparison is the linear fit of the data for $h>10h_{elastic}$ in the constant load and hold tests (Fig. 2.7), which gives a stress exponent $n = 1.12$. It is curious that the data point for the slowest CSR test agrees well with the CLH

data even though the data in Fig. 2.14 suggest that steady state conditions were not achieved for this test. The other discrete CSR data points are also in good agreement with the CLH linear fit with the exception of the highest mean contact pressure, for which the CSR tests give a measurably higher rate. Since the basic experimental data in Fig. 2.14 show that steady conditions were achieved for this test, this deviation may be further indication that there is indeed power-law breakdown and an increase in the stress exponent at higher stresses when the tests are conducted under constant strain rate conditions. The dashed line through the CSR data is a curve fit that is used in the next section to evaluate the stress exponent locally at each data point.

6.5   Comparison of all measurements

In order to compare and assess the data obtained by all the various methods, a plotting scheme is required that allows for a direct comparison of the indentation results to the uniaxial results. One way to achieve this is by algebraic rearrangement of Bower's basic prediction for the indentation creep rate, Eq. 4, to the form:

$$\left(\frac{1}{hc\,tan\,\theta}\right)\left(\frac{dh}{dt}\right) = \alpha\left(\frac{p_{nom}}{c^2 F}\right)^n ,$$
(18a)

which can be further reduced to:

$$\frac{\dot{h}}{a} = \alpha\left(\frac{p_m}{F}\right)^n .$$
(18b)

Comparison of Eq. 18b to the basic creep relation for uniaxial data, Eq. 1, reveals that the uniaxial data plotted as $\dot{\varepsilon}$ vs. σ are directly comparable to the indentation results if the indentation data are plotted as $\dot{h}$/a vs. p_m/F; that is, both plots are exactly of the same power-law form $y = \alpha x^n$. To implement this, it is simply necessary to modify the indentation data by computing a from h using $a = hc\,tan\,\theta$ and p_m from p_{nom} using $p_m = p_{nom}/c^2$. Since c and F are both functions of n, the conversions require an experimental measurement of the value for n. Note that the form of Eq. 18b suggests that there are natural reasons to define the indentation strain rate as $\dot{h}/a$ rather than $\dot{h}/h$.

Using these methods, data from all the various measurement methods are plotted together for comparison in Fig. 2.16 assuming that the stress exponent is fixed at $n = 1.12$. The corresponding values of c and F, which follow from Eqs. 10 and 11 using $\theta = 70°$ and $n = 1.12$, are $c = 0.71$ and $F = 1.07$. The data in the figure demonstrate that the indentation measurements compare well with the uniaxial data when p_m/F or σ is less than about 0.1 GPa. These stresses correspond to the longer time/higher displacement indentation data after the transients have relaxed. Although the two uniaxial data points at higher stresses lie above the indentation data, it should be recalled that these two data points were obtained in tests in which a true steady state was not achieved and the deformation was probably not homogeneous through the gauge length. The tensile viscosity measurements of Stephens also compare favorably to the indentation results in the low stress regime (Stephens, 1978).

The data at higher stresses, which in the indentation tests correspond to shorter creep times and smaller depths of penetration, are more complicated and clearly indicate a load-history dependence. Interestingly, all the constant load and hold tests (CLH) are tightly grouped together and maintain their linear behavior over the entire range on the plot, even though one might expect some deviations based on the effects of the elastic transient and the possibility of higher stress exponents due to power law breakdown. On the other hand, the constant rate of loading tests (CRL) show a marked deviation from linear behavior in the higher stress regime, with the magnitude of the deviation depending on the loading rate. Curiously, at the highest rates, the CRL data are well matched by the constant strain rate tests (CSR). Since the data in Fig. 2.14 indicate that steady state conditions were clearly achieved in the high rate CSR tests, this may be an indication that there is indeed power-law breakdown at higher rates.

An alternative approach to comparing the uniaxial and indentation creep data is to assume that there is not a unique single value of n, as might be expected at the higher mean pressures, but to use the local measurements of n based on the various techniques developed in this work along with the corresponding values of c and F derived from Eqs. 10 and 11 to plot the indentation data. This has been done in Fig. 2.17, using the data in Fig. 2.9 to determine the variation of n with depth in the CLH tests, the data in Fig. 2.12

47

for the CRL tests, and the data in Fig. 2.15 for the CSR tests. At first glance, Fig. 2.17 looks very much like Fig. 2.16, but there are two notable differences. First, in the low stress regime where all the measurement techniques give similar results, the data in Fig. 2.16 are essentially linear on the log-log plot giving a single value of n. On the other hand, the data in Fig. 2.17 show a slight curvature in this regime, which is consistent with a slightly increasing stress exponent as the stress is increased. Second, although the higher stress uniaxial data are very far removed from the rest of the curves in Fig. 2.16, they merge with the higher stress CSR data and faster rate CRL data in Fig. 2.17. As previously noted, the higher stress uniaxial data are suspect due to a lack of steady state conditions, but the fact that they converge so well to some of the indentation data in Fig. 2.17 could be another indication of the importance of power law breakdown at higher stresses. This issue could be resolved by conducting constant stress tests, rather than constant strain rate tests, to obtain a less ambiguous set of uniaxial creep data. Unfortunately, our uniaxial testing apparatus could be used only for constant strain rate tests.

Lastly, we wish to note that although the observations here are encouraging, they are by no means the last word on the value of indentation testing for measuring creep parameters. The material investigated in this study is rather unusual in that, over a significant range of test parameters, it creeps in a relatively history independent fashion with a stress exponent close to one. Most engineering materials used in creep applications exhibit significant loading history effects, lengthy transients produced by microstructural changes, higher stress exponents, and power law breakdown at high stresses. All of these would lead to further complications in the analysis. On the other hand, to the extent that transient behavior becomes less important at long creep times and indentation stresses diminish into the power law range as the indentation contact grows, indentation testing could still prove valuable. Further studies in other materials are needed to prove out the basic concepts.

7.　Conclusions

(1)　Direct comparison of uniaxial compression creep and indentation creep data obtained in amorphous selenium at 35 ℃ shows that the analysis of Bower et al. can be used to derive the basic uniaxial creep parameters α and n in $\dot{\varepsilon} = \alpha \sigma^n$ from indentation creep data. Although prior work has shown how n can be obtained, the results here show that it is also possible to measure the uniaxial creep coefficient α as well.

(2)　Full field finite element simulations for conical indenters show that corrections to Bower's results for the pile-up/sink-in parameter, c, and the reduced contact pressure, F, are needed to account for finite deformation. The corrections are generally small but could be important in some experimental circumstances. Based on the finite element results, simple empirical equations are provided that relate c and F to the indenter angle, θ, and stress exponent, n.

(3)　Experimental results show that Bower's analysis correctly predicts the pile-up sink-in parameter for a material with a stress exponent close to 1.

(4)　Full field finite element simulations show that there is an initial transient in the indentation creep behavior resulting from the influences of elastic deformation. For constant load and hold indentation creep tests, the transient affects the evaluation of the stress exponent for penetration depths up to about ten times the elastic strain. Transient effects on the evaluation of α are more problematic and may extend to larger depths, especially for larger n. The transient is confirmed in experiment.

(5)　Three different indentation methods for measuring α and n have been explored: (i) constant load and hold (CLH), (ii) constant loading rate (CLR), and (iii) constant strain rate (CSR). The methods give very different results at short indentation creep times, but eventually converge to similar results. The initial differences are probably caused by a variety of factors including elastic transients and the influence of power law breakdown on the measurements.

References

Asif, S.A.S., Pethica, J.B., 1997. Nanoindentation creep of single-crystal tungsten and gallium arsenide. Philos. Mag. A 76, 1105-1118.

Atkins, A.G., Silverio, A., Tabor, D., 1966. Indentation hardness and creep of solids. J. Inst. Met. 94, 369-378.

Bower, A.F., Fleck, N.A., Needleman, A., Ogbonna, N., 1993. Indentation of a power law creeping solid. Proc. R. Soc. London Ser. A 441, 97-124.

Bucaille, J.L., Felder, E., Hochstetter, G., 2002. Identification of the viscoplastic behavior of a polycarbonate based on experiments and numerical modeling of the nano-indentation test. J. Mater. Sci. 37, 3999-4011.

Cheng, Y.T., 2001. Scaling relationships in indentation of power-law creep solids using self-similar indenters. Philos. Mag. Lett. 81, 9-16.

Chu, S.N.G., Li, J.C.M., 1977. Impression creep - A new creep test. J. Mater. Sci. 12, 2200-2208.

Etienne, S., Guenin, G., Perez, J., 1979. Ultrasonic studies of the elastic coefficients of vitreous selenium about Tg. J. Phys. D: Appl. Phys 12, 2189-2202.

Fischer-Cripps, A.C., 2004. A simple phenomenological approach to nanoindentation creep. Mater. Sci. Eng. A 385, 74-82.

Grau, P., Berg, G., Meinhard, H., Mosch, S., 1998. Strain rate dependence of the hardness of glass and Meyer's law. J. Am. Ceram. Soc. 81, 1557-1564.

Hill, R., 1992. Similarity analysis of creep indentation tests. Proc. R. Soc. London Ser. A 436, 617-630.

Lee, J.H., Zhou, C., Su, C.J., Gao, Y.F., Pharr, G.M., 2010. Similarity relationships in creep contacts and applications in nanoindentation tests. Mat. Res. Soc. Symp. Proc. 1224, FF07-08.

Li, H., Ngan, A.H.W., 2004. Size effects of nanoindentation creep. J. Mater. Res. 19, 513-522.

Lucas, B.N., Oliver, W.C., 1999. Indentation power-law creep of high-purity indium. Metall. Mater. Trans. A 30A, 601-610.

Lucas, G.E., Pendleton, C., 1982. Time-dependent flow properties from indentation tests. J. Nucl. Mater. 103, 1539-1543.

Mayo, M.J., Nix, W.D., 1988. A micro-indentation study of superplasticity in Pb, Sn, and Sn-38 wt-percent-Pb. Acta Metall. 36, 2183-2192.

Mulhearn, T.O., Tabor, D., 1960. Creep and hardness of metals - a physical study. J. Inst. Met. 89, 7-12.

Ogbonna, N., Fleck, N.A., Cocks, A.C.F., 1995. Transient creep analysis of ball indentation. Int. J. Mech. Sci. 37, 1179-1202.

Oliver, W.C., Pharr, G.M., 1992. An improved technique for determining hardness and elastic-modulus using load and displacement sensing indentation experiments. J. Mater. Res. 7, 1564-1583.

Poisl, W.H., Oliver, W.C., Fabes, B.D., 1995. The relationship between indentation and uniaxial creep in amorphous selenium. J. Mater. Res. 10, 2024-2032.

Potter, M.C., Wiggert, C., 1991. Mechanics of Fluids. Prentice Hall, NJ, 210-222.

Raman, V., Berriche, R., 1992. An investigation of the creep processes in tin and aluminum using a depth-sensing indentation technique. J. Mater. Res. 7, 627-638.

Sargent, P.M., Ashby, M.F., 1992. Indentation creep. Mater. Sci. Technol. 8, 594-601.

Sneddon, I.N., 1965. The relation between load and penetration in the axisymmetric Boussinesq problem for a punch of arbitrary profile. Int. J. Eng. Sci. 3, 47.

Stephens, R.B., 1978. Viscosity and structural relaxation rate of evaporated amorphous selenium. J. Appl. Phys. 49, 5855-5864.

Storakers, B., Larsson, P.L., 1994. On brinell and boussinesq indentation of creeping solids. J. Mech. Phys. Solids 42, 307-332.

Su, C.J., LaManna, J.A., Gao, Y.F., Oliver, W.C., Pharr, G.M., 2010. Plastic instability in amorphous selenium near its glass transition temperature. J. Mater. Res. 25, 1015-1019.

Vedam, K., Miller, D.L., Roy, R., 1966. Elastic constants of selenium in hexagonal and glassy phases. J. Appl. Phys. 37, 3432-3434.

Wang, C.L., Lai, Y.H., Huang, J.C., Nieh, T.G., 2010. Creep of nanocrystalline nickel: A direct comparison between uniaxial and nanoindentation creep. Scr. Mater. 62, 175-178.

Wang, C.L., Zhang, M., Nieh, T.G., 2009. Nanoindentation creep of nanocrystalline nickel at elevated temperatures. J. Phys. D-Appl. Phys. 42, 115405-115412.

Wilkinson, D.S., Ashby, M.F., 1975. Pressure sintering by power law creep. Acta Metall. 23, 1277-1285.

Yang, F.Q., Li, J.C.M., Shih, C.W., 1995. Computer-simulation of impression creep using the hyperbolic sine stress law. Mater. Sci. Eng. A 201, 50-57.
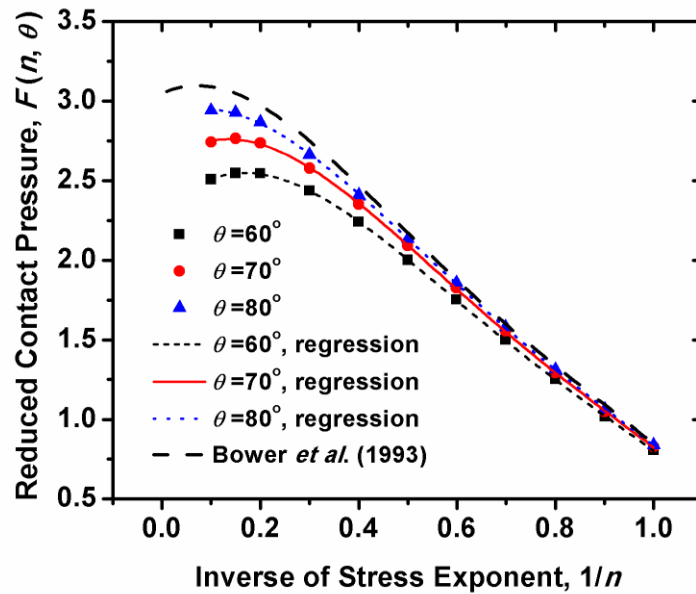
Appendix 2.1.
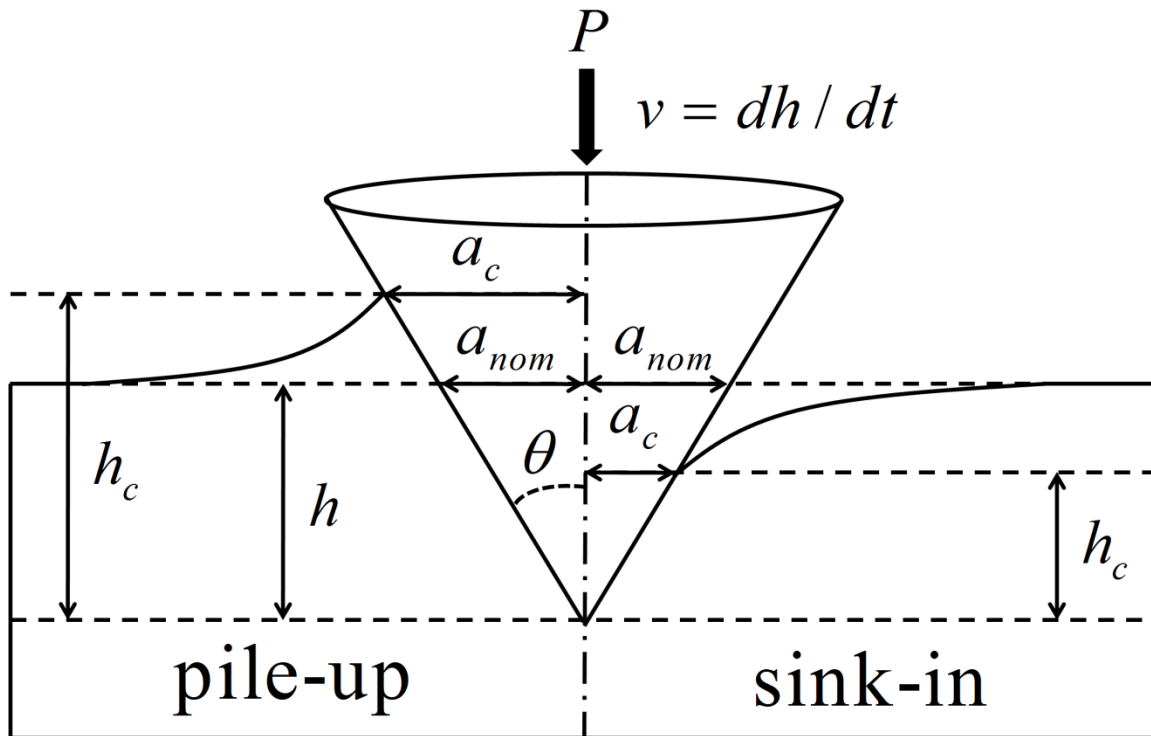
Figure 2.1. Schematic illustration of the contact geometry under load. The left side of the figure shows the configuration when material piles up around the indenter, and the right side when the material sinks-in.
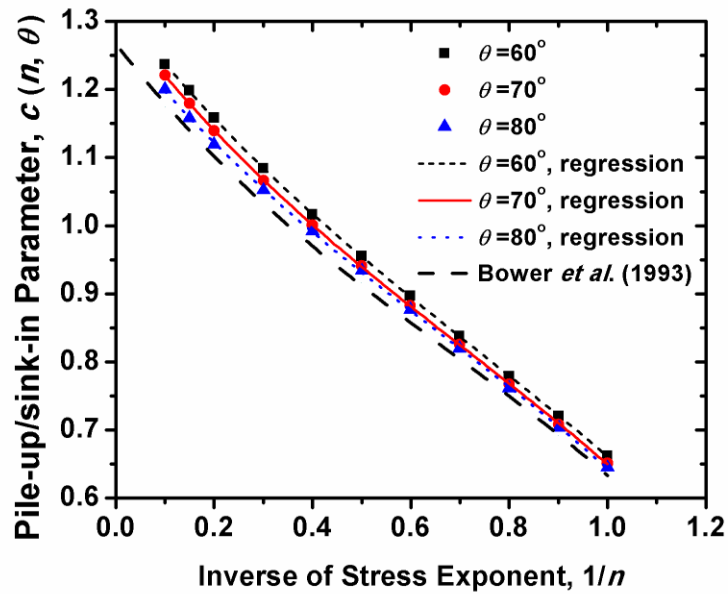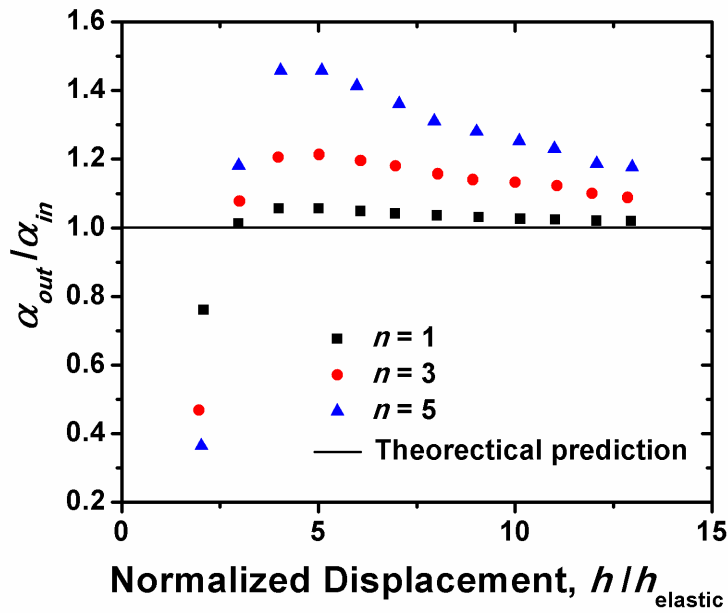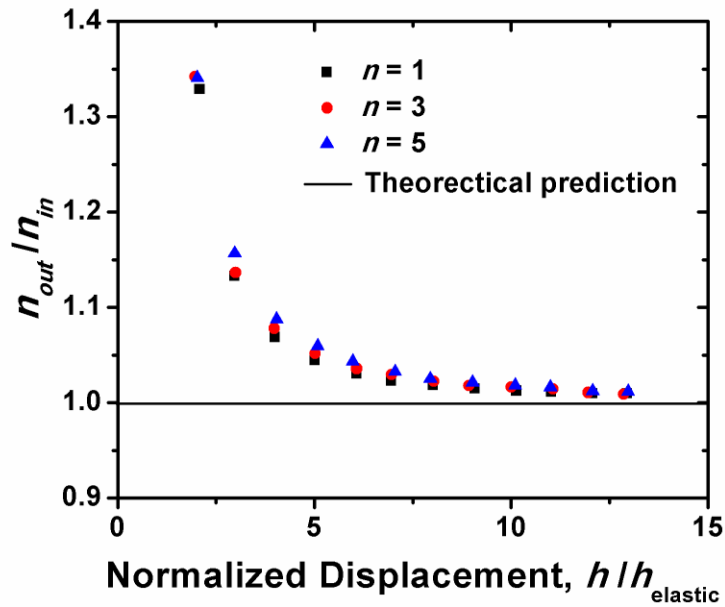
(a)

(b)

Figure 2.2. Finite element results from constant rate of loading simulations (CRL) showing the dependencies of: (a) the pile-up/sink-in parameter, *c*; and (b) the reduced contact pressure, *F*, on the stress exponent, *n* and indenter angle, θ.

(a)

(b)

Figure 2.3. Finite element results from constant rate of loading simulations (CRL) showing the dependencies of the ratios of the output to input values of: (a) the stress exponent, *n*; and (b) the uniaxial creep coefficient, α , on the normalized indenter displacement, $h/h_{elastic}$.
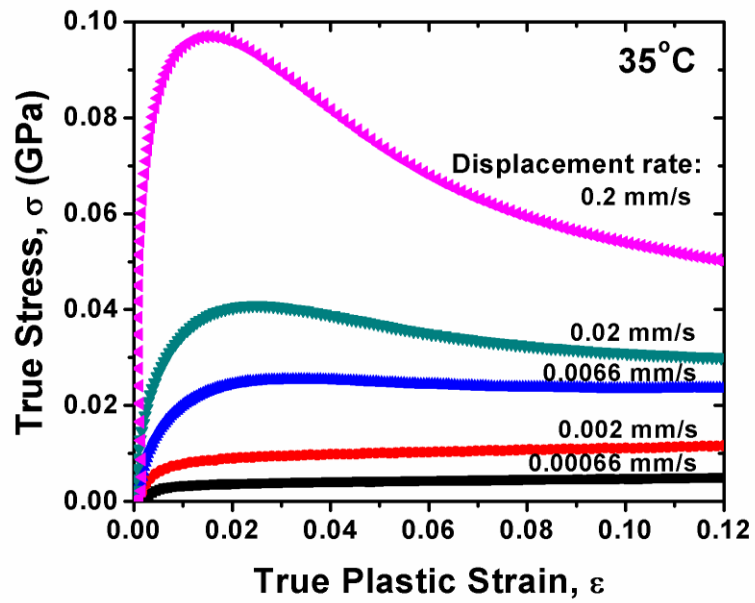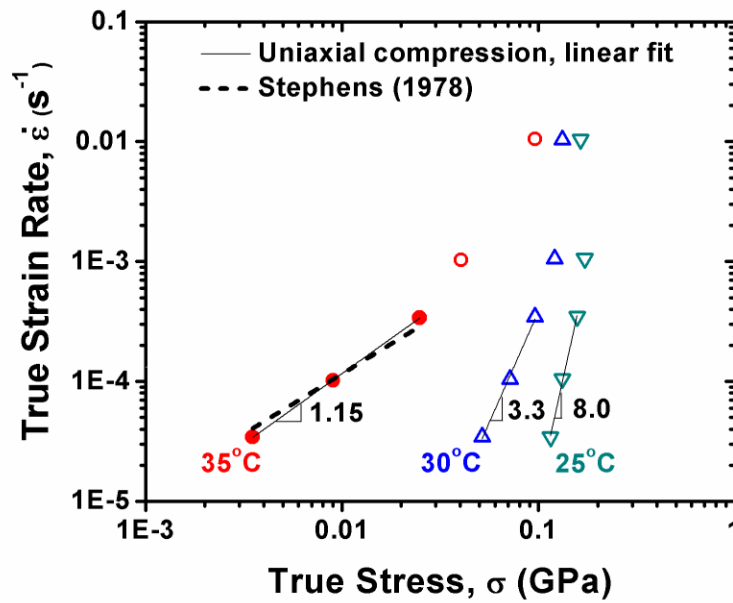
56
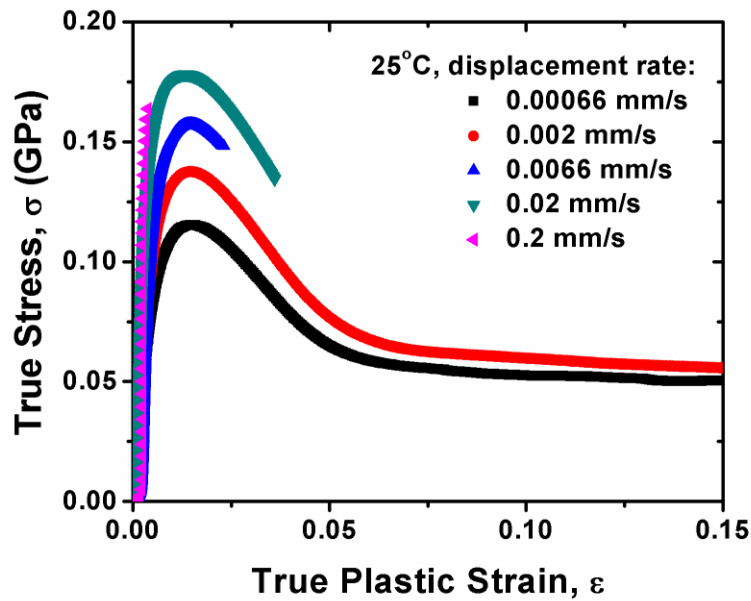
(a)
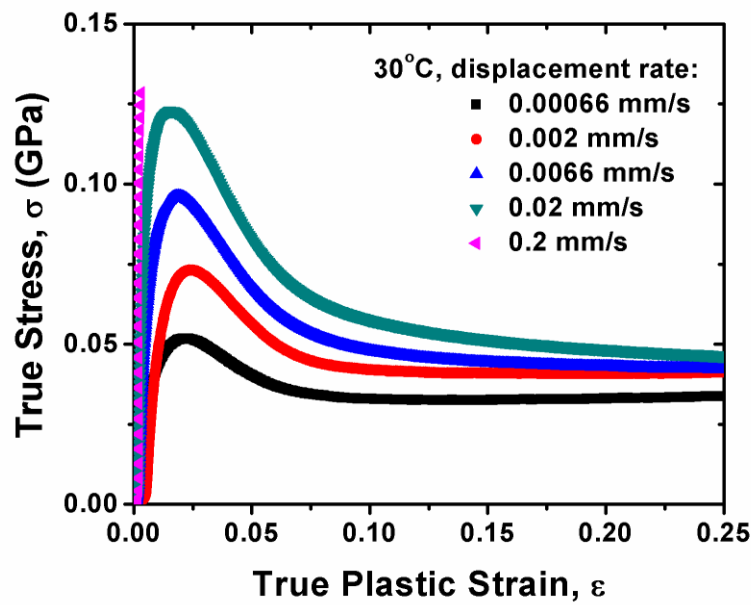
(b)

Figure 2.4. True stress versus true plastic strain curves for amorphous selenium as measured in uniaxial compression tests at constant displacement rates: (a) $T = 25.0$ °C; (b) $T = 30.0$ °C; and (c) $T = 35.0$ °C.

(4)

(c)

Figure. 2.4. Continued

Figure 2.5. True strain rate versus true stress at 2% plastic strain for amorphous selenium as derived from the compression test data in Fig. 2.4. The data of Stephens are based on shear viscosity measurements and the assumption that $n = 1$. Note that only the filled symbols correspond to data believed to be representative of true steady-state conditions.
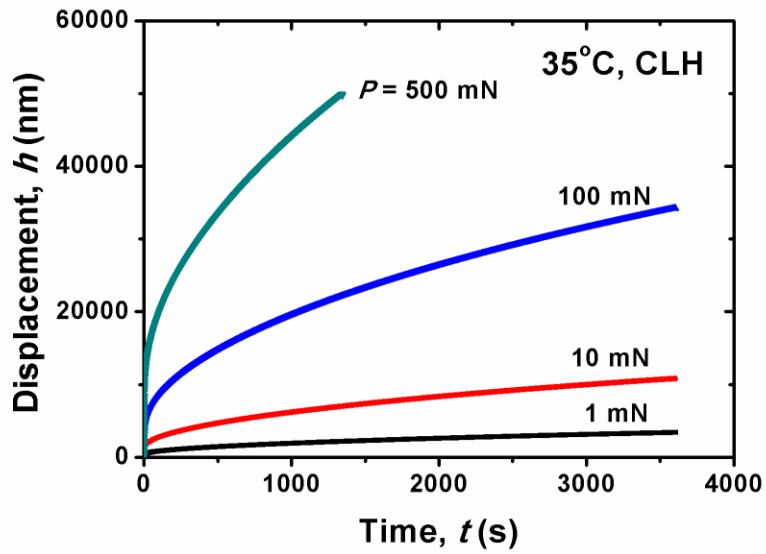
(a)
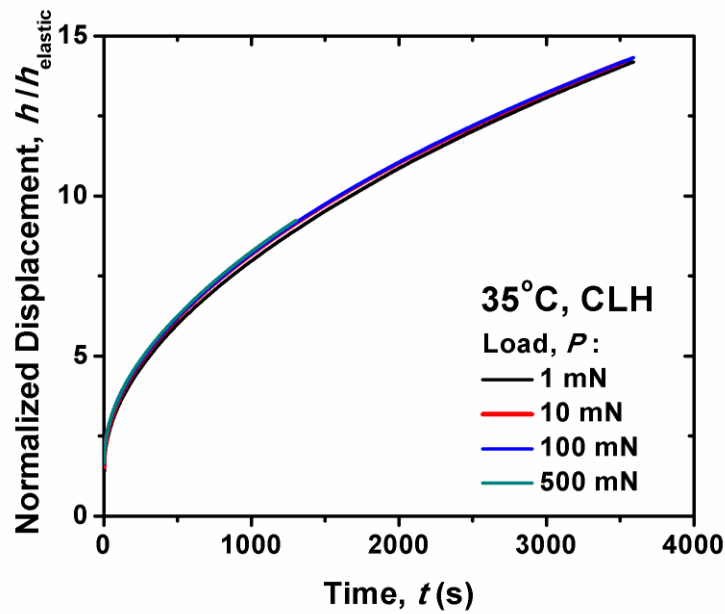
(b)

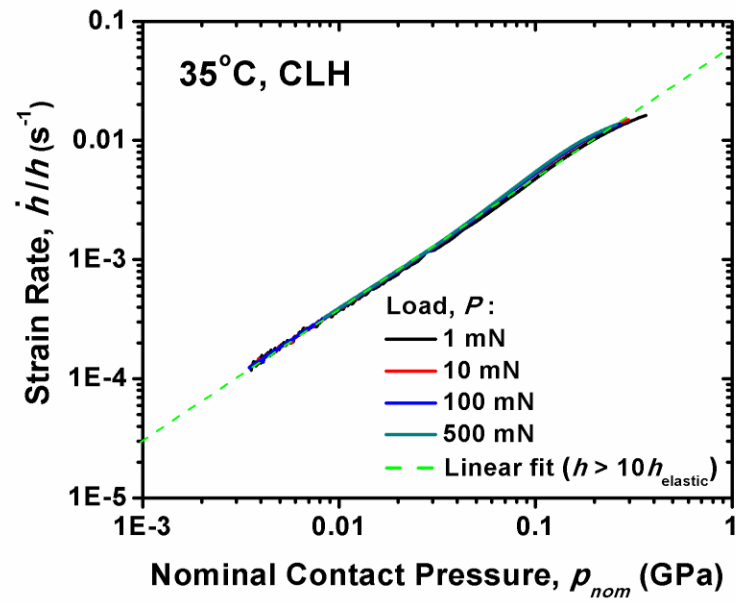**Figure 2.6.** Basic data from constant load and hold indentation creep experiments for amorphous selenium at 35 °C: (a) the displacement-time behavior; and (b) the displacement-time behavior re-plotted with the indenter displacements normalized relative to the elastic displacements, $h_{elastic}$.

Figure 2.7. The data in Fig. 2.6 re-plotted as indentation strain rate vs. nominal contact pressure on log-log axes.
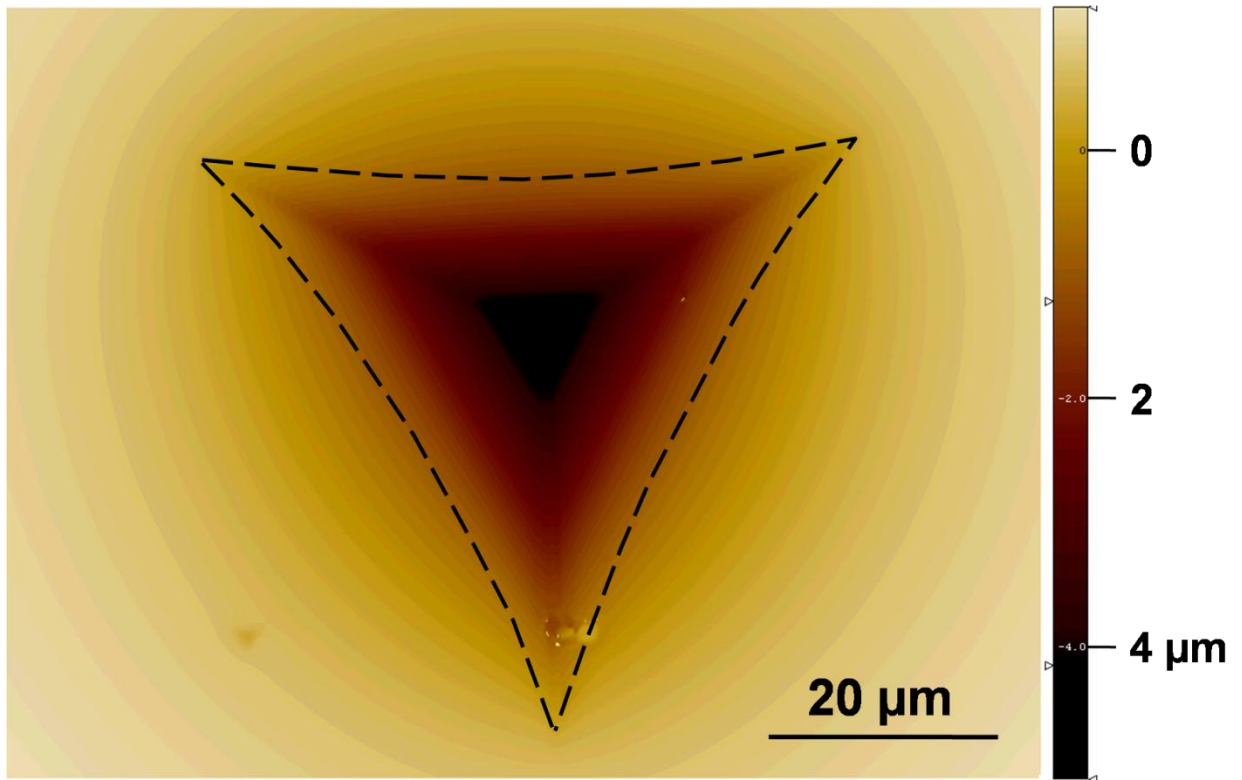
Figure 2.8. An optical micrograph of an indentation made at 35 ℃ using the CLH method obtained using the interferometric surface mapping microscope showing the 3D surface topography. Note that the entire surface is sunk-in around the residual hardness impression and that the sink-in extends well beyond the edges of the micrograph.

(a)

(b)

Figure 2.9. Stress exponents for amorphous selenium obtained from analysis of 35 ℃ constant load and hold *h-t* data evaluated according to the form of Eq. 6: (a) variation of stress exponent with time; and (b) variation of stress exponent with normalized displacement $h/h_{elastic}$.

(a)
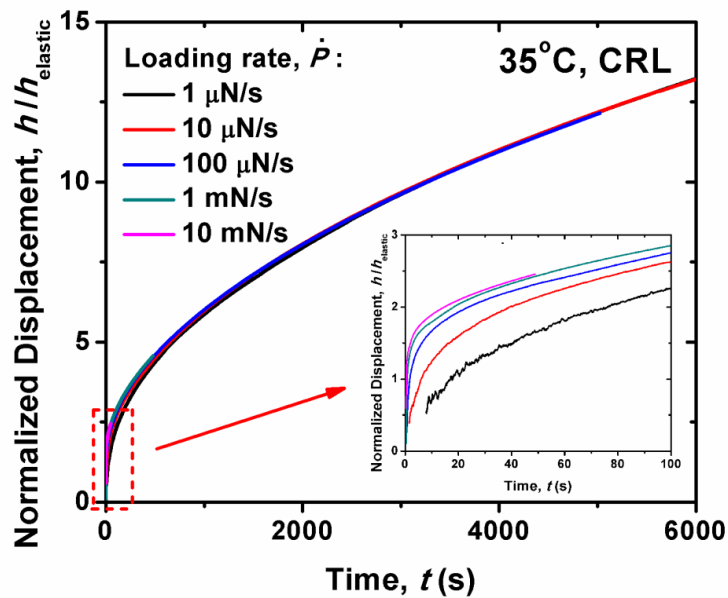
(b)

Figure 2.10. Basic data from constant rate of loading (CRL) experiments for amorphous selenium at 35 °C: (a) the displacement-time behavior; and (b) the displacement-time behavior re-plotted with the indenter displacements normalized relative to the elastic displacements, $h_{elastic}$.
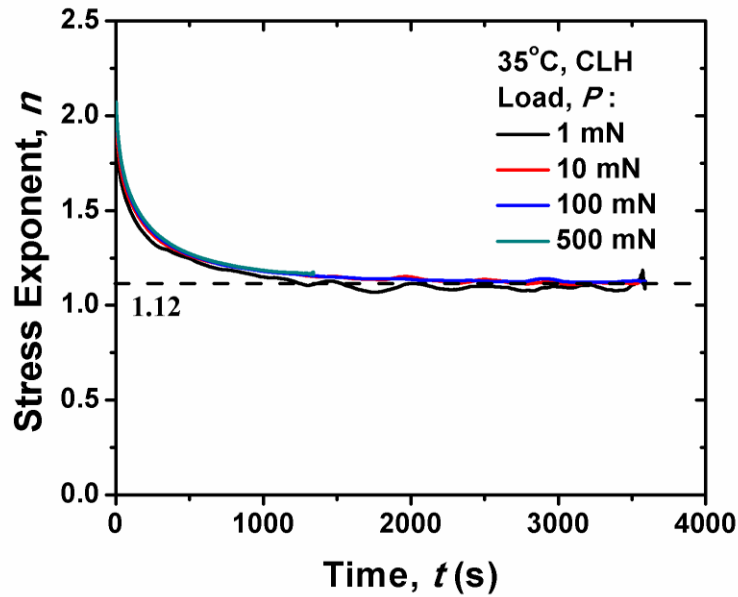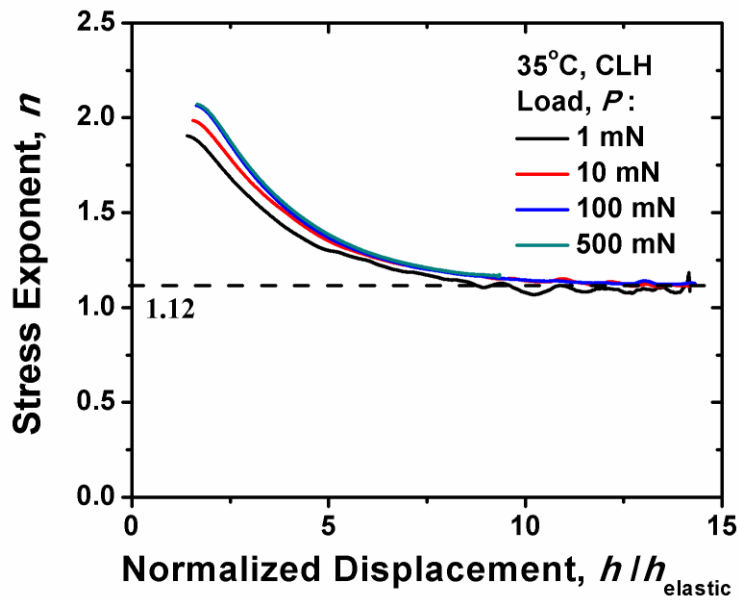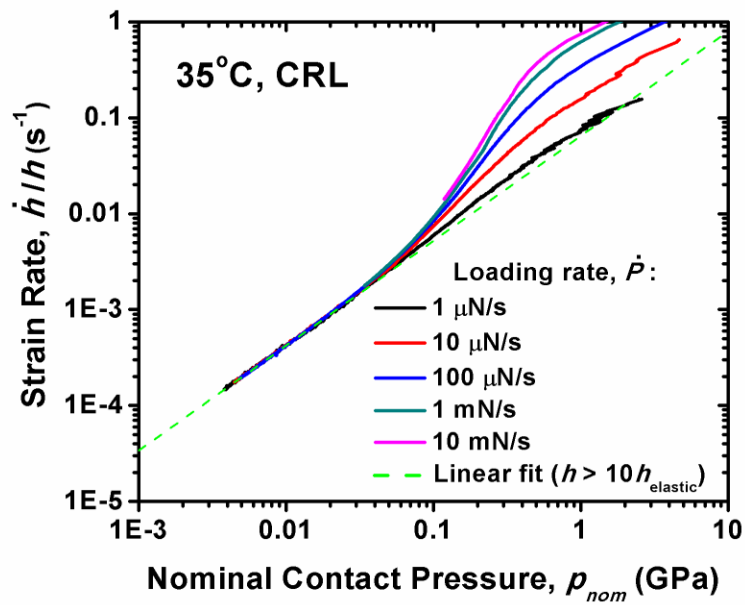
Figure 2.11. The data in Fig. 2.10 re-plotted as indentation strain rate vs. nominal contact pressure on log-log axes.
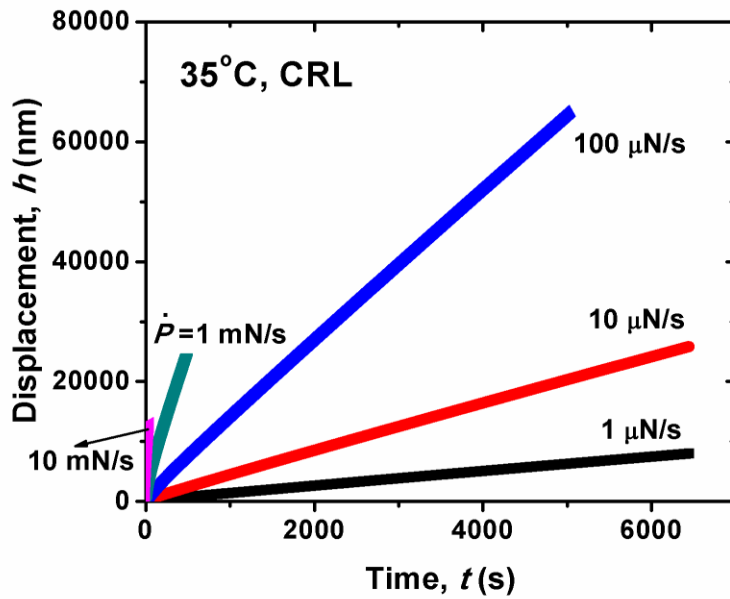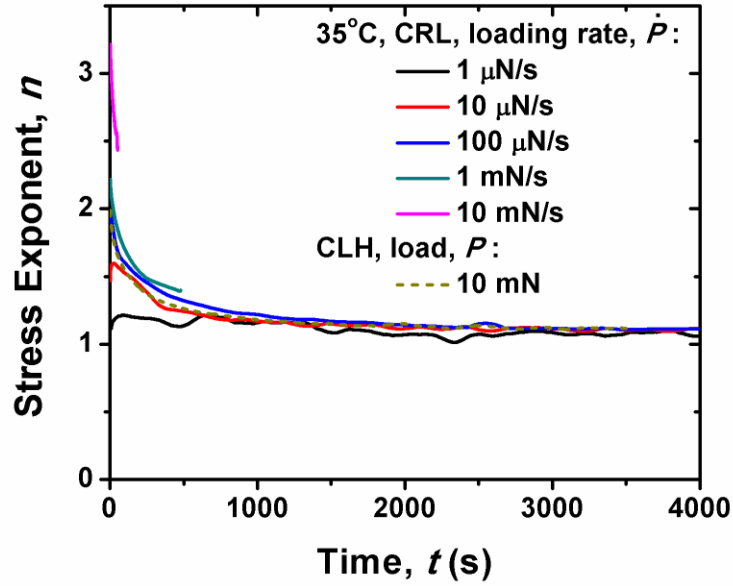
(a)
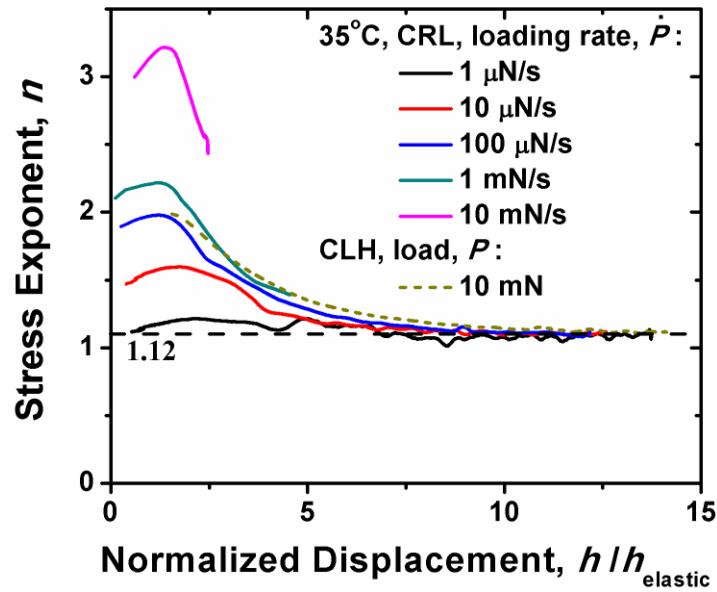
(b)

Figure 2.12. Stress exponents for amorphous selenium obtained from analysis of 35 ℃ constant rate of loading h-t data evaluated according to the form of Eq. 6: (a) variation of stress exponent with time; and (b) variation of stress exponent with normalized displacement $h/h_{elastic}$.

66
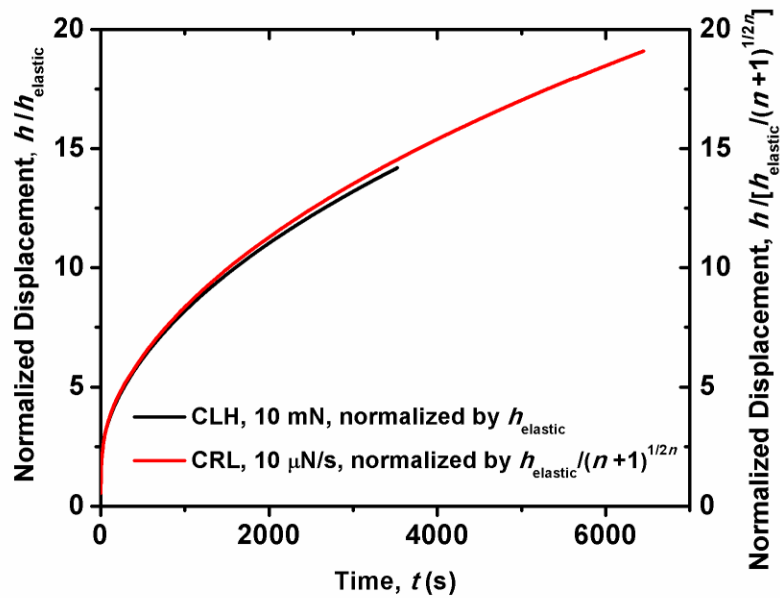
Figure 2.13. Comparison of *h-t* data from a 10 mN constant load and hold test (CLH) to a 10 mN/s constant rate of loading test (CRL) using the displacement normalizations expected to produce convergence. The value *n*=1.12 was assumed for the CRL normalizations.
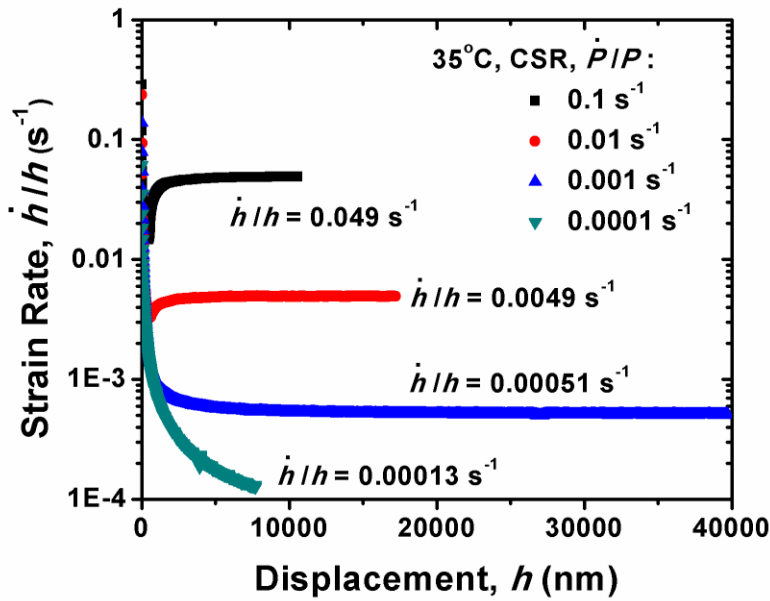
(a)
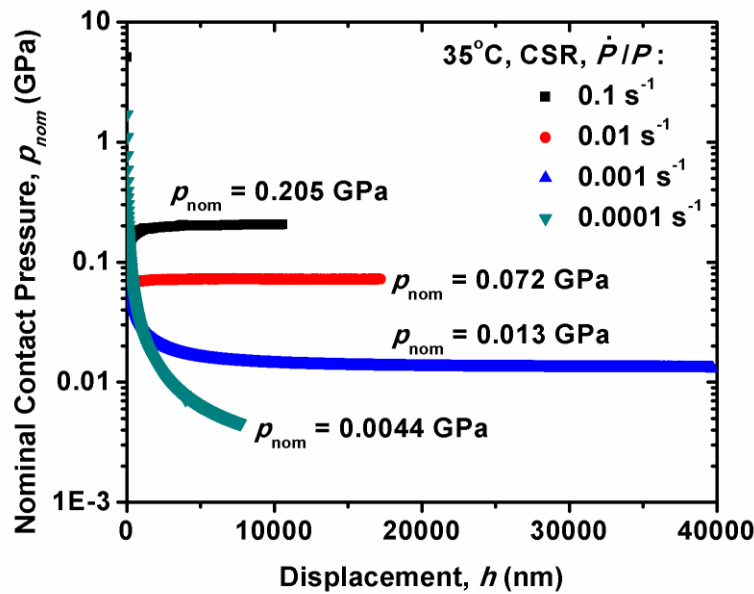
(b)

Figure 2.14. Basic results from constant $\dot{P}/P$ indentation creep experiments (constant strain rate, CSR) conducted at 35 °C: (a) indentation strain rate as a function of displacement; and (b) nominal contact pressure as a function of displacement.
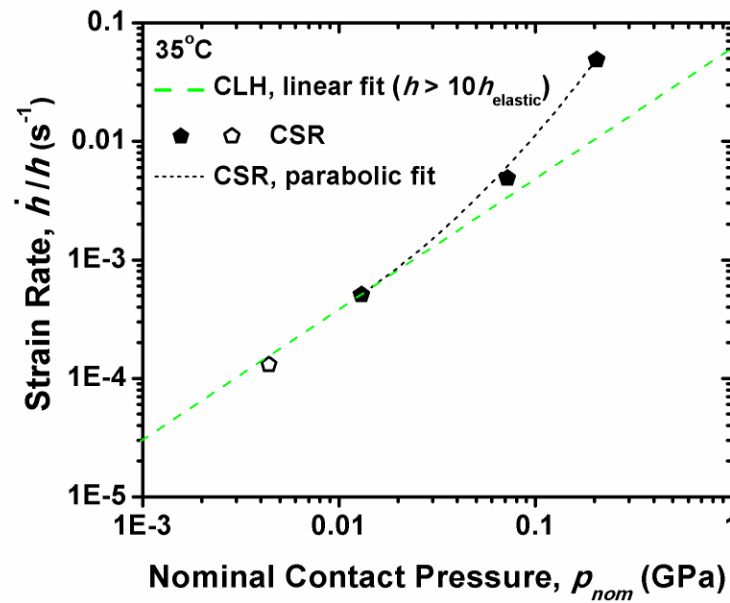
Figure 2.15. The data in Fig. 2.14 re-plotted as indentation strain rate vs. nominal contact pressure on log-log axes. Note that only the filled symbols correspond to data believed to be representative of steady-state conditions.
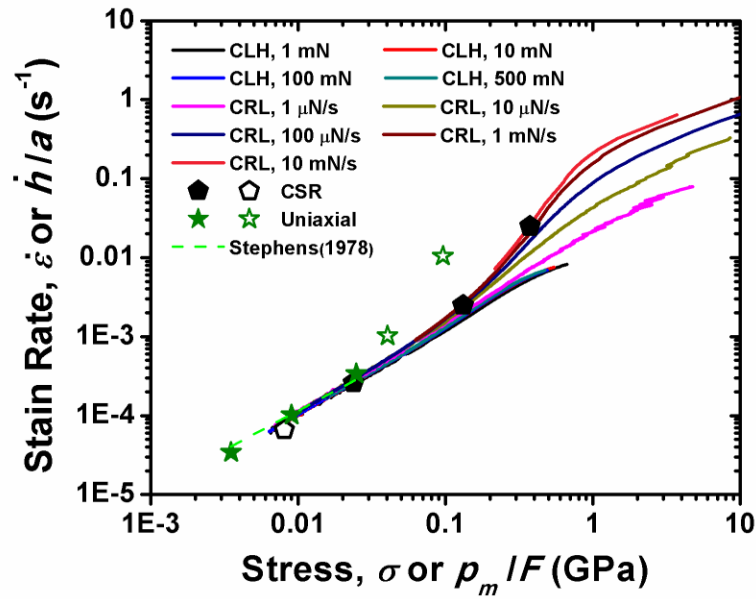
Figure 2.16. Comparison of the strain rate versus stress as determined by uniaxial compression testing, indentation creep, and shear viscosity measurements at 35 °C. The indentation data assume that the creep exponent, n, is fixed at the measured value of 1.12. Stephens shear viscosity data assume $n = 1$. Note that only the filled symbols correspond to data believed to be representative of steady-state conditions.
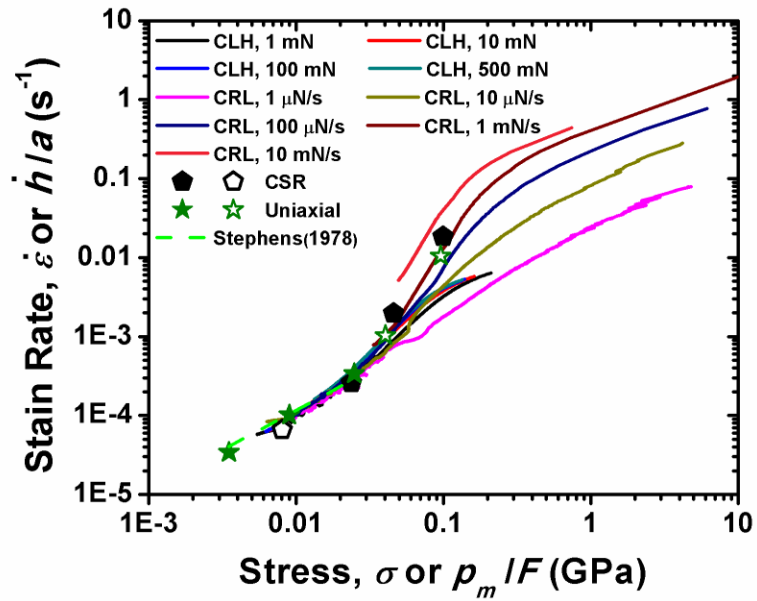
Figure 2.17. The data in Fig. 2.16 re-plotted assuming that n is variable and can be evaluated using the data in Fig. 2.9 for the CLH tests, the data in Fig. 2.12 for the CRL tests, and the data in Fig. 2.15 for the CSR tests.

Table 2.1. Fit parameters for $c\,(n,\,\theta)$ in Eq. 10.

θ	c_0	c_1	c_2	c_3
60 °	1.326	-0.925	0.470	-0.210
70 °	1.310	-0.948	0.540	-0.252
80 °	1.281	-0.884	0.493	-0.247

Table 2.2. Fit parameters for $F(n, \theta)$ in Eq. 11.

θ	F_0	F_1	F_2	F_3	F_4
60 °	2.280	3.496	-13.253	12.349	-4.069
70 °	2.588	2.745	-12.428	11.915	-3.996
80 °	2.889	1.522	-10.242	10.074	-3.407

CHAPTER III
An experimental method for minimizing thermal drift from instrumented indentation creep experiments

This article will be submitted to the *Journal of Materials Research*. It hasn't been published anywhere, nor will it be before I turn in the final version of my ETD, so I didn't include a publication statement.

Authors:

C. J. Su, E. G. Herbert
Dept. of Materials Science and Engineering, University of Tennessee, Knoxville, TN 37996

W. C. Oliver
Nanomechanics Inc., Oak Ridge, TN 37830

G. M. Pharr
Dept. of Materials Science and Engineering, University of Tennessee, Knoxville, TN 37996; and Materials Science and Technology Division, Oak Ridge National Lab, Oak Ridge, TN 37831

Abstract

New analysis methods, based on Bower's analysis and Sneddon's indentation stiffness equation, are proposed to extract the uniaxial power-law creep parameters α and n from instrumented indentation creep experiments with continuous stiffness techniques in a manner that minimizing the influence of thermal drift. Experimental verification of the proposed methods is provided through constant load and hold indentation creep experiments performed with a Berkovich indenter on amorphous selenium at 35 ℃, which generates a contact geometry that initially exhibits significant pile-up followed by a gradual transition to sink-in behavior. Results shows that the proposed techniques, which rely on the measured stiffness rather than the displacement, can be used to accurately predict the projected contact area and the basic uniaxial creep parameters α and n based on an assumed value of Young's modulus and Poisson's ratio for the material. The proposed methods were then applied to indentation creep data obtained in high purity polycrystalline aluminum with n~5 at 250 ℃, in which thermal drift caused by localized heating of the sample was very large. The uniaxial creep parameters α and n of aluminum determined by the proposed techniques are generally in good agreement with previously published results, thus demonstrating the validity of the approach.

1.   Introduction

Thermal drift is one of the most significant obstacles in measuring reliable displacement data during an instrumented indentation creep experiment (Asif and Pethica, 1997; Goldsby et al., 2004; Hay et al., 2010; Li and Bhushan, 2002; Oliver and Pharr, 1992, 2004; Rar et al., 2005). Since the strain rate and stress both depend on the displacement of the indenter as a function of time, any contribution from drift to the displacement directly manifests itself as an error in the predicted creep properties. The magnitude of the error in displacement depends solely on the drift rate, the elapsed time, and the total depth. In reasonably well-controlled laboratory conditions, the thermal drift rate during an indentation test is typically less than 0.1 nm/s. When it can be demonstrated that the product of the measured drift rate and elapsed time is a small fraction of the total depth, then the contribution of thermal drift can safely be ignored. Alternatively, the displacement data can potentially be corrected by subtracting the contribution of drift from the total depth. These methods, however, assume that the measured drift rate is constant over the duration of the test. Because this assumption becomes less and less reliable as the testing time increases, the measured displacement during a creep test is particularly vulnerable to contributions from thermal drift that may or may not be accurately removed. Additional complications can also arise with the implementation of Peltier type specimen heating stages, which are frequently used to achieve high temperatures in the sample. Consider, for example, the experimental data presented in Fig.1, which show the displacement-time response recorded during indentation creep experiment performed on an aluminum sample that was heated to 250 °C by a localized heating stage. The data were obtained from a constant load and hold creep test performed with a Berkovich diamond indenter that was loaded to 10 mN in 2 s. Following the load ramp, the peak load was maintained constant for approximately 1800 s during which time the creep displacement were measured as a function of time. The circuitous path of the measured displacement is the direct result of the tip and sample not being maintained at the same constant temperature. These data clearly show that without controlling the temperature of both the sample and the tip, the displacement data taken on

aluminum at 250 °C are completely unreliable due to extreme thermal drift. While simultaneously heating the tip and sample represents ideal experimental conditions, many commercially available systems do not offer this functionality. To combat the detrimental effects of thermal drift, previous investigators have pointed out that the implementation of dynamic nanoindentation techniques can be used to directly measure the elastic contact stiffness in a manner that is effectively independent of drift (Asif and Pethica, 1997; Goldsby et al., 2004; Hay et al., 2010; Li and Bhushan, 2002; Oliver and Pharr, 1992, 2004; Rar et al., 2005). Dynamic methods, such as the continuous stiffness measurement (CSM) technique, are typically insensitive to thermal drift because they operate on a time scale (frequencies of 45 Hz or higher) that is much faster than the rate at which nominal drift rates can affect the measured displacement. Thus, the goal of this investigation was to explore whether or not the detrimental effects of thermal drift in instrumented indentation creep experiments can be mitigated or eliminated by relying on a known elastic modulus and direct measurement of the elastic contact stiffness rather than the displacement into the surface of the sample.

Recently published work by the authors demonstrated the ability of a constant load and hold indentation creep experiment to accurately predict the uniaxial constitutive creep parameters of amorphous selenium at 35 °C (Su et al., 2012; Su et al., 2010). The analysis is based on a simple power law relation between the steady state creep rate, $\dot{\varepsilon}$, and the applied stress, σ,

$$\dot{\varepsilon} = \alpha\sigma^n ,$$ (1)

where α and n are the constitutive creep parameters as measured in uniaxial tension or compression. The values of α and n predicted from the indentation experiments were based on an analysis of Bower et al. and measurements of the indentation load, P, depth, h, and time, t (Bower et al., 1993). A critical assessment of the proposed method was made by developing a plotting scheme to directly compare the indentation and uniaxial results, which were shown to match very well within the limit of steady-state deformation. Thus, the author's previously published work provides the theoretical and experimental underpinning of this investigation. The fundamentals of Bower's analysis

and the details of the relations between indentation and uniaxial creep are left to the author's previously published work and will only be revisited here where deemed necessary.

2.   Application to instrumented indentation testing

Regardless of the source of thermal drift, the net effect is that it adds a component to the measured displacement that can only be accurately removed if the measured drift rate is constant over the duration of the test. We propose that even when this condition cannot be met, that direct, continuous measurement of the elastic contact stiffness, S, can be used to accurately determine the true projected contact area, A, and ultimately the $\dot{\varepsilon}$ and σ that are used to determine the values of α and n. To do so, however, requires prior knowledge of the elastic modulus and Poisson's ratio of the sample.

Among of the fundamental equations in nanoindentation is Sneddon's stiffness equation:

$$S = \frac{2}{\sqrt{\pi}} \beta^* E^* \sqrt{A} \; , \tag{2}$$

which relates S to the projected contact area, A, through β^*, a geometric constant taken to be 1.034 for the Berkovich, and E^*, the reduced or indentation modulus which is related to Young's modulus by:

$$E^* = \left(\frac{1-v_i^2}{E_i} + \frac{1-v_s^2}{E_s} \right)^{-1} \; , \tag{3}$$

where v_i, v_s, E_i, and E_s are Poisson's ratio and Young's modulus of the indenter and the sample, respectively (Pharr et al., 1992; Sneddon, 1965).It follows then from Eqs. 2 and 3 that if S is measured as a continuous function of time and the elastic properties of the tip and sample are known, then A can be directly calculated from S completely independent of h. The true mean contact pressure, $p_m = P/A$, then in terms of the measured S, is given by

$$p_m = \frac{P}{A} = \frac{4P}{\pi}\left(\frac{\beta^* E^*}{S}\right)^2 . \tag{4}$$

As these relations show, the significant advantage of implementing dynamic nanoindentation methods is that it allows direct determination of A largely independent of thermal drift and it requires absolutely no assumptions about the contact geometry, specifically, the amount of pile-up or sink-in. The same can also be said of p_m as long as P is held constant by compensating the applied load to account for the displacement of the indenter column working against the support springs.

The indentation strain rate, $\dot{\varepsilon}_i$, is defined as $\dot{h}/h$. Since the measured parameters of the proposed method are P, S, and t, rather than P, h, and t, an equivalency must be generated to relate P, S, and t to $\dot{h}/h$. This can be accomplished by assuming the indenter tip area function is that of a perfect Berkovich, i.e., $A = 24.56h_c^2$, and utilizing Bower's pile-up/sink-in parameter, c, which is simply the proportionality constant between the contact depth, h_c, and the indentation depth h:

$$c = h_c / h . \tag{5}$$

Through the assumed area function and Eqs. 2 and 5, algebraic manipulation allows $\dot{\varepsilon}_i$ to be recast in terms of h_c, c, and S as:

$$\dot{\varepsilon}_i = \frac{\dot{h}}{h} = \frac{\dot{h}_c}{h_c} - \frac{\dot{c}}{c} = \frac{\dot{S}}{S} - \frac{\dot{c}}{c} . \tag{6}$$

Eq. 6 provides the required equivalency and clearly shows that $\dot{h}/h$ is only equivalent to $\dot{S}/S$ in the limit of geometric similarity. In other words, the proposed method can only be used to reliably estimate $\dot{\varepsilon}_i$ when c is constant.

3. Experimental procedures

The validity of the proposed method was assessed using constant load and hold instrumented indentation creep experiments performed in amorphous selenium at 35 °C

and polycrystalline aluminum at 250 °C. Selenium is a suitable model material for this investigation because its glass transition temperature, T_g, is 31.0 ±0.5 °C, and it creeps in very well defined way at slightly higher temperatures (e.g., 35 °C) (Poisl et al., 1995). Thus, simple modifications of commercially available indentation and uniaxial tension/compression systems could be used to characterize the creep behavior without the complications of conducting very high temperature tests. Specific details of the sample processing technique have been described elsewhere (Su et al., 2010). The tests were conducted with an MTS Nano Indenter XP equipped with a Berkovich diamond indenter. The continuous stiffness measurement (CSM) technique was used to measure the elastic contact stiffness as a function of depth and/or time. Details of the CSM technique have been well documented elsewhere (Asif and Pethica, 1997; Goldsby et al., 2004; Hay et al., 2010; Li and Bhushan, 2002; Oliver and Pharr, 1992, 2004; Rar et al., 2005). The CSM system was driven by a phase-lock amplifier (PLA) at 45 Hz and the target set point for the harmonic displacement was 4 nm. Details of the selenium experiments were described in a previous publication (Su et al., 2012; Su et al., 2010). The aluminum sample was 99.999% pure, measured 10 mm in diameter by 4 mm thick, and the average grain size was approximately 200 μm. The Al surface was prepared using SiC grinding papers through 4000 grit followed by 24 hours in an automatic vibratory polishing machine with a polishing suspension of 0.05 μm alumina slurry (γ-Al_2O_3) and a final step of 24 hours with 0.02 μm Buehler MasterMet®2 non-crystallizing colloidal silica (SiO_2). The polished Al disk was mounted to MTS' Localized High Temperature Stage using Cronatron's Poly-2000, a high temperature adhesive rated to approximately 1100° C. Through thermocouples adhered to the surface of the sample, the temperature of the stage was controlled such that the Al surface was maintained at 250 ± 0.1 °C throughout the duration of the tests. The loading was controlled such that the peak load was achieved during a 2 s linear ramp. Following the load ramp, the peak load was maintained constant for approximately 1800 s. Critical assessments of the Se and Al results obtained by the proposed method were based on three important metrics: 1) direct comparison to the author's previously published experimental results obtained in Se at 35 °C, where the

measured displacement was shown to be reliable; 2) direct comparison to the optically measured contact areas determined by measurement with an optical interference microscope; and 3) direct comparison to previously published creep data in Al at 250 °C.

4. Results and discussion

4.1 Indentation creep testing of amorphous selenium at 35 °C

The displacement data acquired during the Se experiments are taken to be free of thermal drift because the entire testing system was maintained at thermal equilibrium (Su et al., 2012). Thus, the validity of the proposed method is explored by making direct comparisons between parameters determined from the measured S and h. The h-t data presented in Fig. 3.2 are previously published results obtained from constant load and hold experiments conducted at 1, 10, 100 and 500 mN (Su et al., 2012). Figure 3a shows the simultaneously measured S as a function of h. The sharp peak in S displayed in each data set is an experimental artifact resulting from the PLA's inability to control the oscillation amplitude during and immediately following the 2 s load ramp. The magnitude of the artifact scales with the peak load because it reflects the change in S incurred during the load ramp. Figure 3b shows the oscillation amplitude versus time during the first 60 s of the experiment. The stiffness measured by the PLA is only reliable when the oscillation amplitude is constant with depth, as the PLA was configured to rely on displacement feedback to control the force required to achieve and maintain the target amplitude of 4 nm. Assuming 90% of the target amplitude represents a minimum S reliability criteria, then the data in Fig. 3.3b show that the measured S is only valid for times and depths greater than approximately 25 s and 14 μm, respectively. Although not shown in the plot, the time required to reach 90% of the target amplitude was observed to be independent of the peak load.

In the limit of geometric similarity, c can be used to relate h_c and h, and, thus, provide a means to compare the measured and predicted value of the ratio S/h. From the

author's previously published results, c during steady state creep of Se at 35 °C is taken to be 0.69. Solving Eq. 2 for A and recognizing $A = 24.56(0.69h_c)^2$ yields:

$$\frac{S}{h} = \frac{2c\beta^* E^*}{\sqrt{\pi/24.56}} = 3.59\beta^* E^* \; . \tag{7}$$

Assuming $\beta^* = 1.034$ and $E^* = 10.2 \; GPa$, then $S/h = 4.03 \times 10^{10} (N/m^2)$ (Etienne et al., 1979; Vedam et al., 1966). The green dashed line emanating from the origin in Fig. 3.3a represents the expected slope of S/h. As the data show, immediately following the sharp peak in S, there is an offset region within each data set that gradually transitions to the expected behavior. This observation becomes clearer when the axes are normalized using the elastic displacement, $h_{elastic}$, which for a conical indenter is given by (Sneddon, 1965)

$$h_{elastic} = \sqrt{\frac{\pi P}{2E^* \tan\theta}} \; , \tag{8}$$

where θ is the half-included and the elastic contact stiffness, $S_{elastic}$, which is derived by substituting $h_{elastic}$ for h in Eq. 7, is given by

$$S_{elastic} = \frac{2\beta^* E^*}{\sqrt{\pi/24.56}} h_{elastic} = \frac{\beta^* E^*}{0.1788} h_{elastic} \; . \tag{9}$$

Through Eqs. 7 and 9, taking the ratio of $S/S_{elastic}$ to $h/h_{elastic}$ yields the magnitude of c. As shown in Fig. 3.3c, when h and S are normalized by Eqs. 8 and 9, respectively, the data collapse to a single master curve that clearly illustrates the deviation from and gradual transition to the expected slope based on the assumption of geometric similarity. Rather than this transition being caused by an initial elastic transient, we hypothesize that this deviation is due to instantaneous plasticity and the breakdown of geometric similarity. Using an interferometric surface mapping microscope, profiles through the residual hardness impressions shown in Fig. 3.4 illustrate the evolution of the contact geometry with time. Immediately following the 2 s load ramp (hold time = 0 s) the contact exhibits significant pile-up at the center of the indent's faces. Within 30 s, however, there is little no evidence of pile-up in the profile of the residual hardness impression and by the end of the test, 3600 s, the contact exhibits significant sink-in both at the center of the indent's

faces and the indent's corners. These observations of the contact geometry support our hypothesis and provide a simple physical explanation for the deviation between the measured and expected value of S/h. This conclusion may also have important implications regarding the determination of α and n, as the breakdown of geometric similarity may coincide with a transition in the pressure distribution as well.

Figure 5a shows A versus h and provides direct evidence that the true contact area calculated from the measured S is reliable. The plotted areas were determined using three different methods: 1) Eq. 2, which depends on the measured S and assumed values of β^* and E^*, 1.034 and 10.2 GPa, respectively, 2) optical measurements of the residual hardness impressions, and 3) the measured h, which relies on Eq. 5, a constant value of c, 0.69, and the assumption of a perfect area function. The excellent correlation between the areas determined from the measured S and the optical measurements of the residual hardness impressions provides direct evidence that S can be used to reliably estimate A through Eq. 2 and the known E^*. The red line, on the other hand, represents the areas calculated from h and Eq. 5, where $c = 0.69$. As expected, the data clearly show that the constant value of c cannot be used to accurately predict A as a function of depth. Additional proof that c is depth dependent can also be given by calculating c based on h and h_c determined from S and the assumed area function. The value of c in this calculation would be the average value of the pile-up/sink-in parameter for a pyramidal indenter. The result of this calculation is represented by the solid black line plotted in Fig. 3.5b, which shows c versus h, and as the data show, c is indeed depth dependent in a manner that is consistent with the profiles through the residual hardness impressions shown in Fig. 3.4. This result is further corroborated by comparing to the value of c determined by the optically measured areas and the assumed area function. The result of this calculation is represented by the individual star data points.

Figure 6a shows the measured h and h_c versus t, where h_c is calculated from S and the assumed area function. Based on the calculated values of c, these data are consistent with our expectations because h_c is always less than h due to sink-in. When the value of c determined from the optically measured areas (Fig. 3.5b) is used to determine h from h_c, Fig. 3.6b shows the correlation is excellent. This result provides additional experimental

84

evidence that proves the validity of the assumed area function and corroborates the breakdown of geometric similarity at shallow depths. Collectively, the results presented in Fig.'s 3-6 demonstrate the ability of the proposed method to reliably predict the true projected contact area from the direct, continuous measurement of the elastic contact stiffness. These results also show that because of instantaneous plasticity, the constant load and hold creep test can generate a contact geometry that evolves and gradually transitions to become geometrically similar with depth.

The indentation strain rate versus the true mean contact pressure is shown in Fig. 3.7. The individual star data points form the basis of an important comparison because they were determined from the measured h and the optically measured values of c as a function of depth (Fig. 3.5). The solid lines represent the data calculated directly from the measured P, S, and t data and Eq. 2 assuming $E^* = 10.2$ GPa. As the data show, both methods generate similar results at lower strain rates and stresses. The increasing deviation between the two methods at higher strain rates and stresses is attributed to the lack of geometric similarity and the resulting change in c with depth or other transients. The increase in slope at higher pressures and higher strain rates, on the other hand, is not well understood and has several potential explanations. Among them are elastic transients, a breakdown of steady-state behavior, and an evolving pressure distribution caused by the instantaneous plasticity incurred by the 2 s load ramp. At the lower stresses and strain rates, the data are reasonably linear and consistent with the results presented in the author's previously published work.

4.2   Indentation creep testing of polycrystalline aluminum at 250 °C

In comparison to Se, Al provides a more realistic depiction of how the proposed test method would be used in practice, as the sample is heated using a localized heating stage, and n is no longer 1, but ~ 5. In addition to being representative of structural engineering materials, Al's creep behavior is also well documented. Thus, Al is an excellent reference material that can be used to test the validity of the proposed method. Figure 1 illustrates the h-t response of Al at 250 °C and shows the commonly used

experimental setup generates displacement data that are completely inconsistent with basic expectations. After the initial sudden increase in depth of ~ 1,500 nm, the data show the indenter quickly moves backwards ~ 3,700 nm followed by yet another reversal of the direction and the gradual recovery of ~ 1200 nm. If the system were at or near thermal equilibrium, then the measured displacement is nominally expected to increase with time. As these data clearly show, the system is nowhere near thermal equilibrium and, therefore, the measured displacement data are completely unreliable. Fig. 3.8a shows representative S-t data that were simultaneously recorded with the displacement data shown in Fig. 3.1. The oscillation amplitude is shown in Fig. 3.8b and, as expected, for t ≥ 25 s the amplitude is within ~ 90% or better of the 4 nm target. This observation is consistent with the Se results and indicates the S data are reliable following the initial peak that has previously been identified as an experimental artifact caused by the 2 s load ramp. The single discrete data point shown in Fig. 3.8a at 1800 s was calculated using Eq. 2, an assumed E^* of 65.7 GPa at 250 °C, and A determined from optical measurements of the residual hardness impression (Gerlich and Fisher, 1969). The value of c determined from the measured A was 1.03, indicating the contact exhibits a small amount of pile-up. The good correlation between the single data point and the measured S indicates the data are consistent with our expectations based on the experimental observations made in Se at 35 °C.

Fig. 3.9 shows $\dot{\varepsilon}_i$ as a function of p_m. The axes were calculated from the measured P, S, and t data, thus, $\dot{\varepsilon}_i$ is taken to be $\dot{S}/S$ and p_m is calculated using Eq. 2 and the assumed E^* of 65.7 GPa. Without reliable h data or three-dimensional images of the contact geometry as a function of depth, it is not possible to objectively evaluate the extent to which c may or may not be depth dependent. Because the data in Fig. 3.9 are reasonably linear, at least for the large creep times, it is assumed the contact can be idealized as geometrically similar with depth and, thus, c is taken to be constant. Comparison between the indentation data and results previously reported in the literature is best accomplished by directly plotting $\dot{\varepsilon}$ versus σ. For reasons described in the author's previously published work, to do so requires that the indentation p_m be

86

normalized by Bower's reduced contact pressure, F, and $\dot{\varepsilon}_i$ be recast in terms of $\dot{h}/a$, where a is the contact radius. The magnitude of F is taken to be a unique function of n and the indenter geometry. From the data presented in Fig. 3.9, $n = 4.6$. The characteristic feature of the indenter geometry is its equivalent cone angle, which for the Berkovich is 70.3°. Through analysis presented in the author's previously published work and these inputs, F is found to be 2.71. To recast $\dot{\varepsilon}_i$ in terms of $\dot{h}/a$ is only a matter of geometry. Assuming c is constant, then the correlation between $\dot{\varepsilon}$ and σ can be expressed accordingly:

$$\frac{\dot{S}}{S}\frac{1}{c\tan\theta} = \frac{\dot{h}}{h}\frac{1}{c\tan\theta} = \frac{\dot{h}}{a} = \alpha\left(\frac{p_m}{F}\right)^n , \tag{10}$$

where θ is the equivalent cone angle of the Berkovich. Calculated in accordance with Eq. 10 and assuming $c = 1.03$, Fig. 3.10 shows $\dot{\varepsilon}$ versus σ for the indentation data and three sets of previously published results from the literature (Luthy et al., 1980; Straub and Blum, 1990; Weertman, 1956). Table 3.1 shows the values of n and α obtained from each data set. Despite differences in the estimated values of n and α, the data in Fig. 3.10 clearly show reasonably good correlation between all four data sets and, thus, provides initial experimental verification of the proposed method.

5.   Conclusions

(1)   A constant load and hold indentation creep experiment performed with a 2 s load ramp in amorphous selenium at 35 °C generates a contact geometry that initially exhibits significant pile-up followed by a gradual transition to sink-in behavior. Despite the loss of geometric similarity, the recorded P, S, and t data can be used in conjunction with Sneddon's stiffness equation to accurately predict the projected contact area based on an assumed value of Young's modulus of the sample.

(2)   Defining the indentation strain rate as $\dot{S}/S$ is equivalent to $\dot{h}/h$ only in the limit of geometric similarity, meaning Bower's pile-up/sink-in parameter, c, must be

constant with depth. When the measured displacement is not reliable, this condition can only be confirmed to the extent that a plot of $\dot{S}/S$ versus p_m is linear.

(3) Despite extreme thermal drift caused by localized heating of the sample, direct comparison of previously published results and indentation creep data obtained in polycrystalline aluminum at 250 ℃ shows that the analysis of Bower et al. can be used to derive the basic uniaxial creep parameters α and n in $\dot{\varepsilon} = \alpha\sigma^n$. Although prior work has shown that it is possible to do so based on the measured load, depth, and time data recorded during an indentation creep test, the results here show that it is also possible to predict the creep properties based on continuous stiffness techniques that rely on the measured stiffness rather than the displacement.

References

Asif, S.A.S., Pethica, J.B., 1997. Nanoindentation creep of single-crystal tungsten and gallium arsenide. Philos. Mag. A-Phys. Condens. Matter Struct. Defect Mech. Prop. 76, 1105-1118.

Bower, A.F., Fleck, N.A., Needleman, A., Ogbonna, N., 1993. Indentation of a power law creeping solid. Proc. R. Soc. London Ser. A-Math. Phys. Eng. Sci. 441, 97-124.

Etienne, S., Guenin, G., Perez, J., 1979. Ultrasonic studies of the elastic coefficients of vitreous selenium about Tg. J. Phys. D: Appl. Phys 12, 2189.

Gerlich, D., Fisher, E.S., 1969. High temperature elastic moduli of aluminum. J. Phys. Chem. Solids 30, 1197-1205.

Goldsby, D.L., Rar, A., Pharr, G.M., Tullis, T.E., 2004. Nanoindentation creep of quartz, with implications for rate- and state-variable friction laws relevant to earthquake mechanics. J. Mater. Res. 19, 357-365.

Hay, J., Agee, P., Herbert, E., 2010. Continuous stiffness measurement during instrumented indentation testing. Exp. Tech. 34, 86-94.

Li, X.D., Bhushan, B., 2002. A review of nanoindentation continuous stiffness measurement technique and its applications. Mater. Charact. 48, 11-36.

Luthy, H., Miller, A.K., Sherby, O.D., 1980. Stress and temperature-dependence of steady-state flow at intermediate temperatures for pure polycrystalline aluminum. Acta Metallurgica 28, 169-178.

Oliver, W.C., Pharr, G.M., 1992. An improved technique for determining hardness and elastic-modulus using load and displacement sensing indentation experiments. J. Mater. Res. 7, 1564-1583.

Oliver, W.C., Pharr, G.M., 2004. Measurement of hardness and elastic modulus by instrumented indentation: Advances in understanding and refinements to methodology. J. Mater. Res. 19, 3-20.

Pharr, G.M., Oliver, W.C., Brotzen, F.R., 1992. On the generality of the relationship among contact stiffness, contact area, and elastic-modulus during indentation. J. Mater. Res. 7, 613-617.

Poisl, W.H., Oliver, W.C., Fabes, B.D., 1995. The relationship between indentation and uniaxial creep in amorphous selenium. J. Mater. Res. 10, 2024-2032.

Rar, A., Sohn, S., Oliver, W.C., Goldsby, D.L., Tullis, T.E., Pharr, G.M., 2005. On the measurement of creep by nanoindentation with continuous stiffness techniques. Mater. Res. Soc. Symp. Proc. 841, 119-124.

Sneddon, I.N., 1965. The relation between load and penetration in the axisymmetric Boussinesq problem for a punch of arbitrary profile. Int. J. Eng. Sci. 3, 47.

Straub, S., Blum, W., 1990. Does the natural 3rd power law of steady-state creep hold for pure aluminum. Scr. Metall. Materialia 24, 1837-1842.

Su, C.J., Herbert, E.G., Sohn, S., LaManna, J.A., Oliver, W.C., Pharr, G.M., 2012. Measurement of power-law creep parameters by instrumented indentation methods. J. Mech. Phys. Solids.

Su, C.J., LaManna, J.A., Gao, Y.F., Oliver, W.C., Pharr, G.M., 2010. Plastic instability in amorphous selenium near its glass transition temperature. J. Mater. Res. 25, 1015-1019.

Vedam, K., Miller, D.L., Roy, R., 1966. Elastic constants of selenium in hexagonal and glassy phases. J. Appl. Phys. 37, 3432-3434.
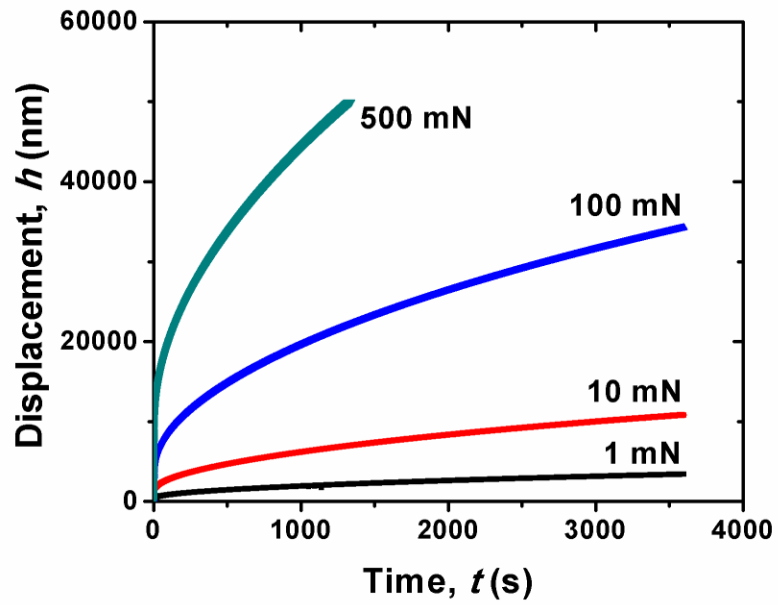
Weertman, J., 1956. Creep of polycrystalline aluminium as determined from strain rate tests. J. Mech. Phys. Solids 4, 230-234.
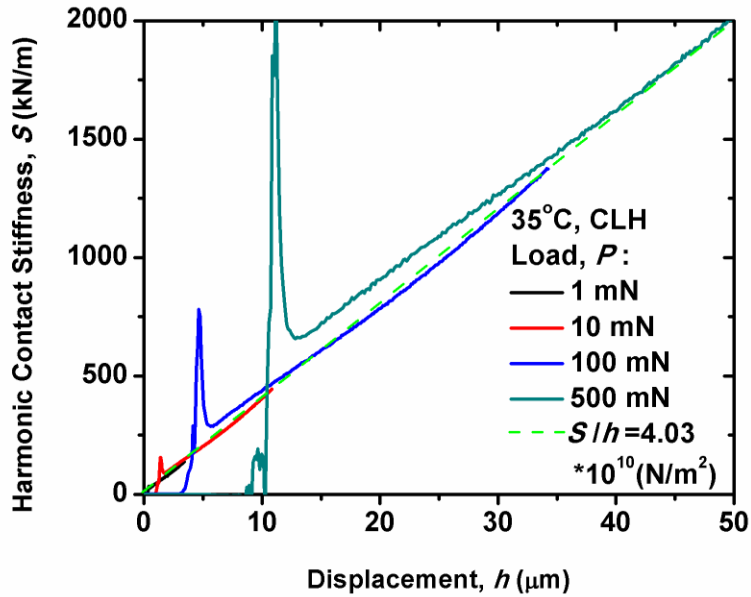
Appendix 3.1.
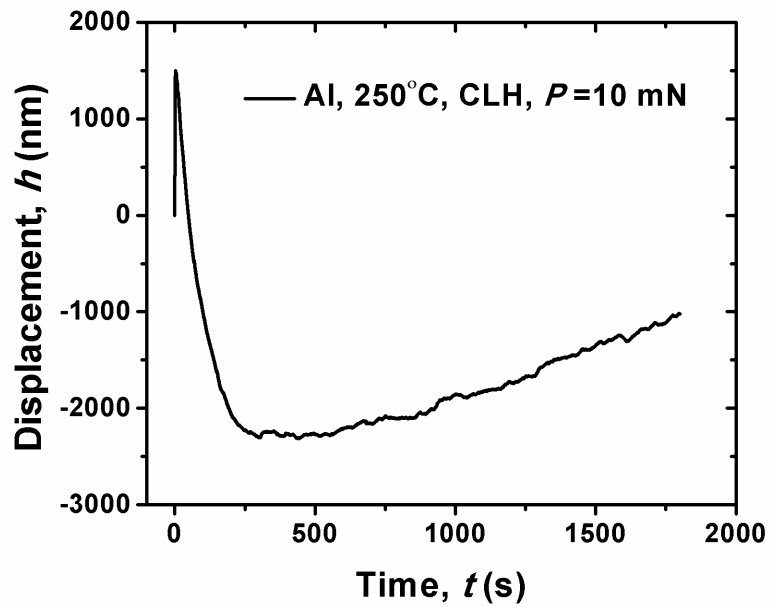
Figure 3.1. The displacement versus time behavior from constant load and hold indentation creep experiments for high purity aluminum at 250 ℃ using the MTS Localized High Temperature Stage.

Figure 3.2. The displacement versus time behavior from constant load and hold indentation creep experiments for amorphous selenium at 35 ℃.

(a)

Figure 3.3. Basic data from constant load and hold indentation creep experiments for amorphous selenium at 35 °C: (a) the harmonic contact stiffness vs. displacement behavior; (b) the harmonic displacement vs. time and displacement behavior for $P = 500$ mN; and (c) the harmonic contact stiffness vs. displacement behavior re-plotted with the indenter harmonic contact stiffness and displacements normalized relative to the elastic harmonic contact stiffness, $S_{elastic}$, and the elastic displacements, $h_{elastic}$, respectively.
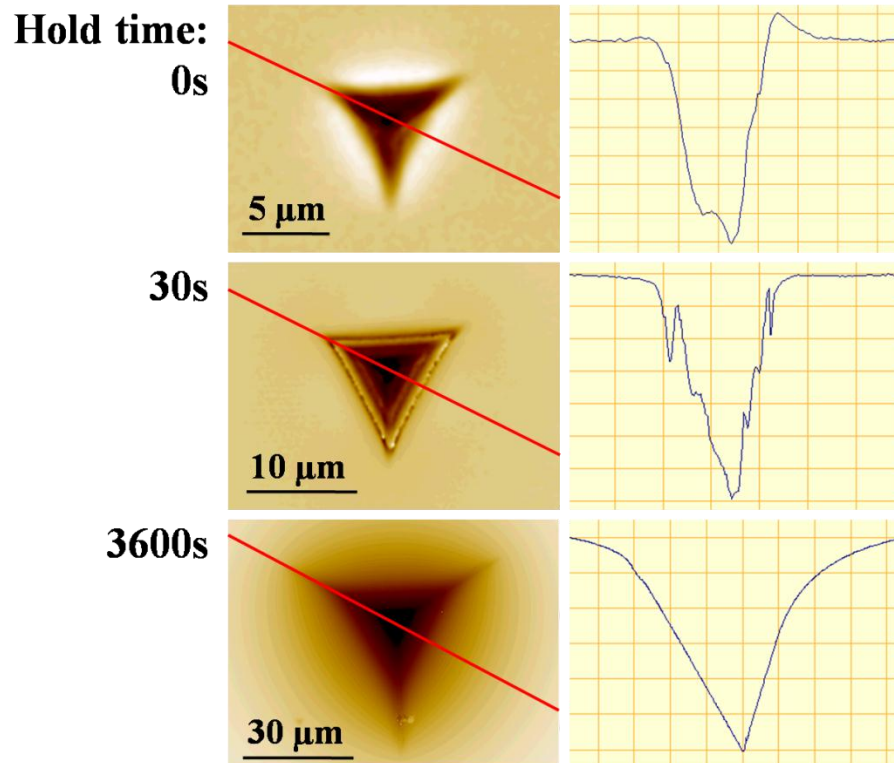
94
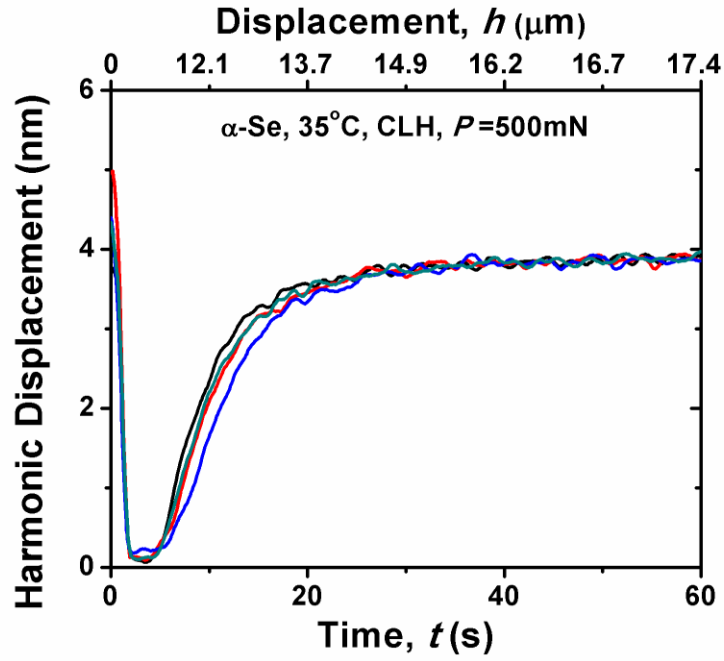
(b)
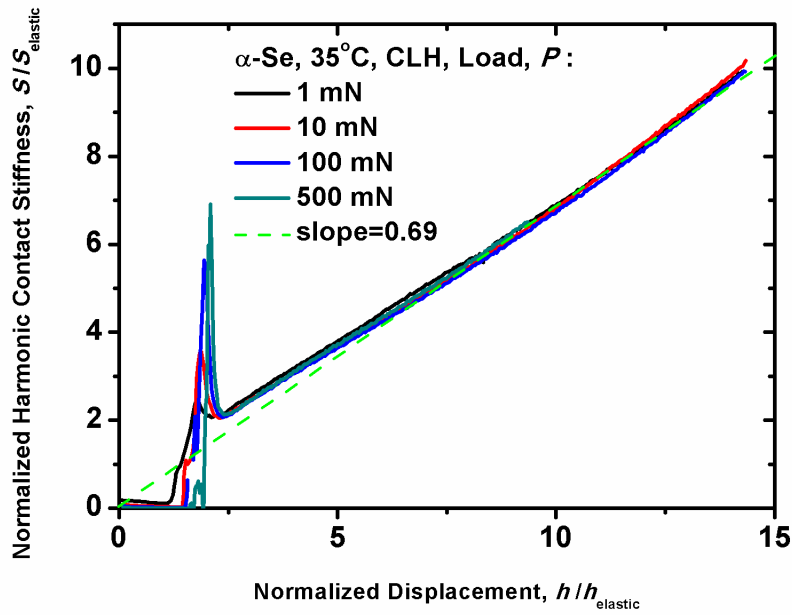
(c)

Figure 3.3. continued

Figure 3.4. The optical micrographs of indentation made at 35 °C with P = 10 mN using the CLH method obtained using the interferometric surface mapping microscope showing the 3D surface topography and line profile for hold time: 0 s, pile-up; 30 s, no pile-up; 3600 s, significant sink-in. Note that for 3600 s hold time the entire surface is sunk-in around the residual hardness impression and that the sink-in extends well beyond the edges of the micrograph.
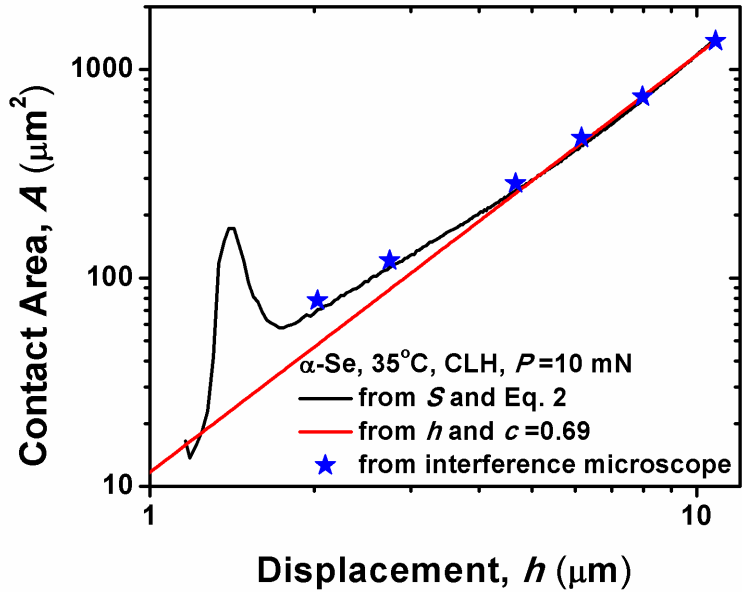
(a)
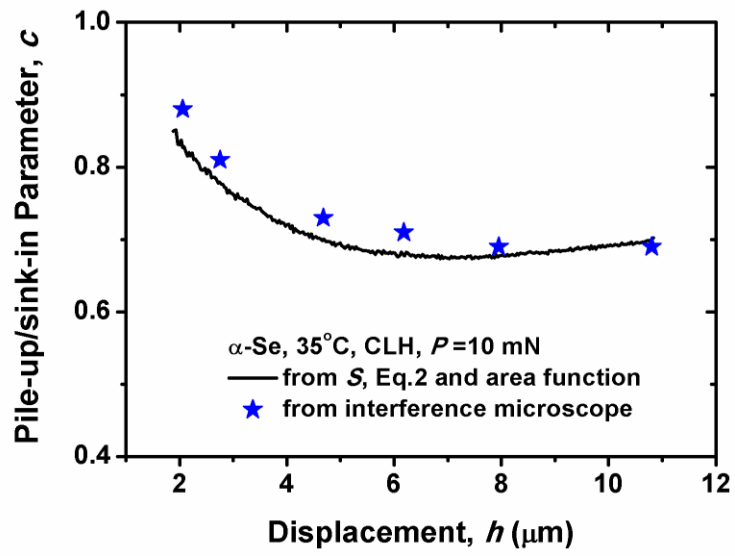
(b)

Figure 3.5. The data in Fig. 3.3 for $P = 10$ mN re-plotted as: (a) the indentation contact area vs. displacement on log-log axes using either the stiffness equation, perfect Berkovich indenter geometry, or interference microscope measurement; and (b) the indentation pile-up/sink-in parameter vs. displacement using either the stiffness equation or interference microscope measurement.
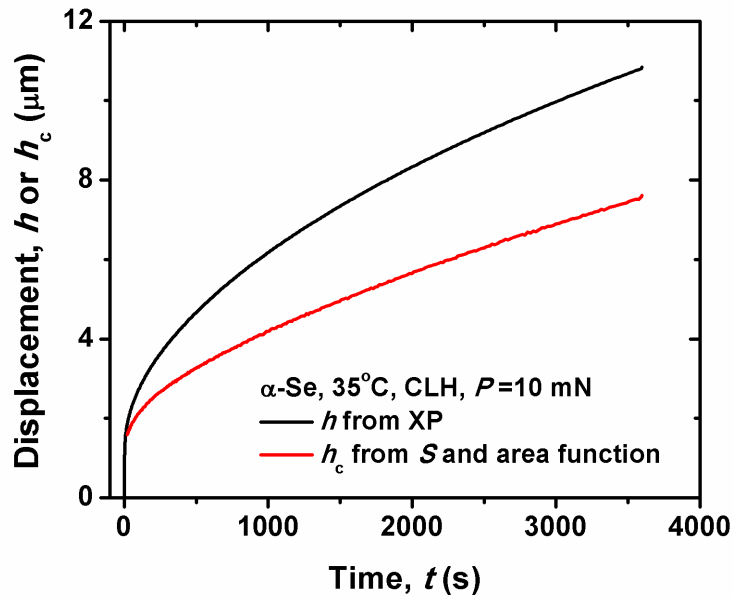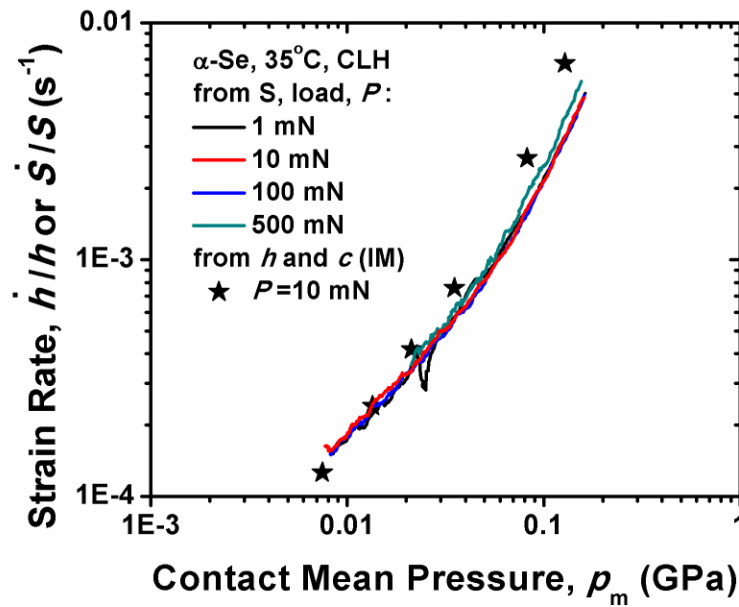
(a)
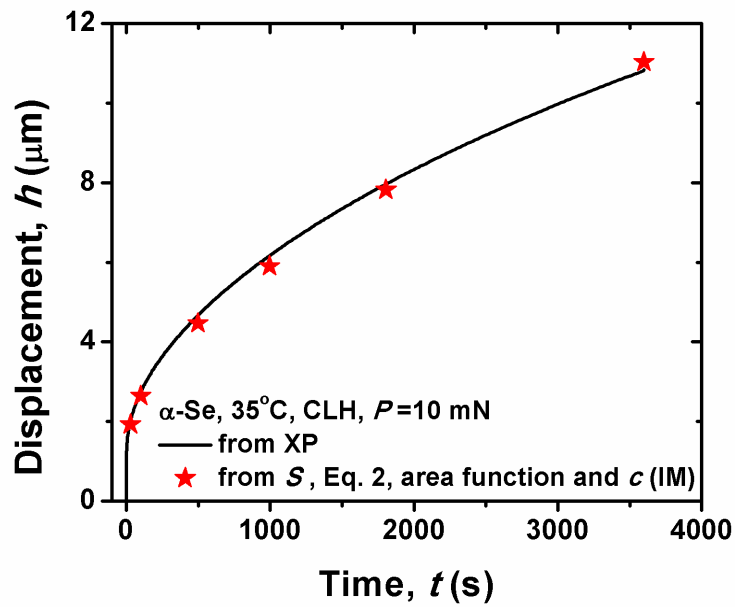
(b)

Figure 3.6. The data in Fig. 3.5 re-plotted as: (a) the indentation contact displacement; and (b) the indentation displacement calculated from measured harmonic contact stiffness, comparing with the measured displacement as a function of time.

98

Figure 3.7. The indentation strain rate vs. nominal contact pressure from the indentation displacement and harmonic contact stiffness by constant load and hold indentation creep experiments for amorphous selenium at 35 ℃ on log-log axes.
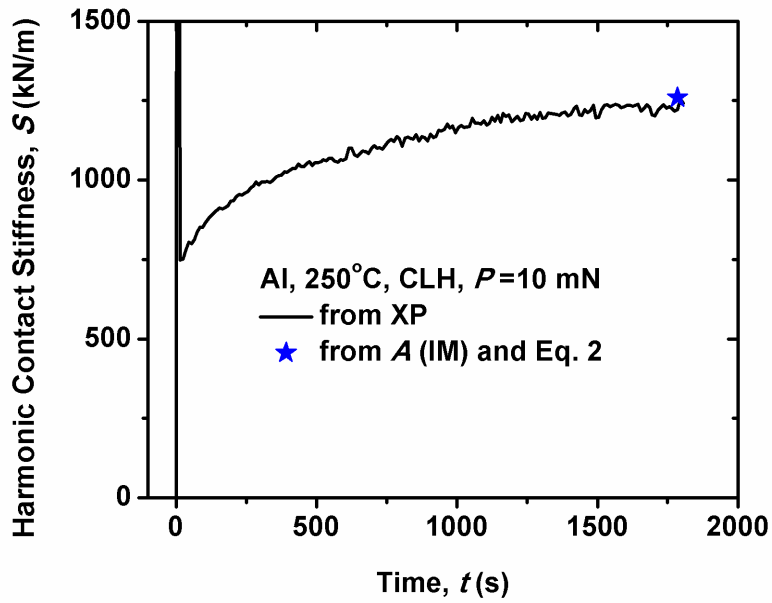
(a)
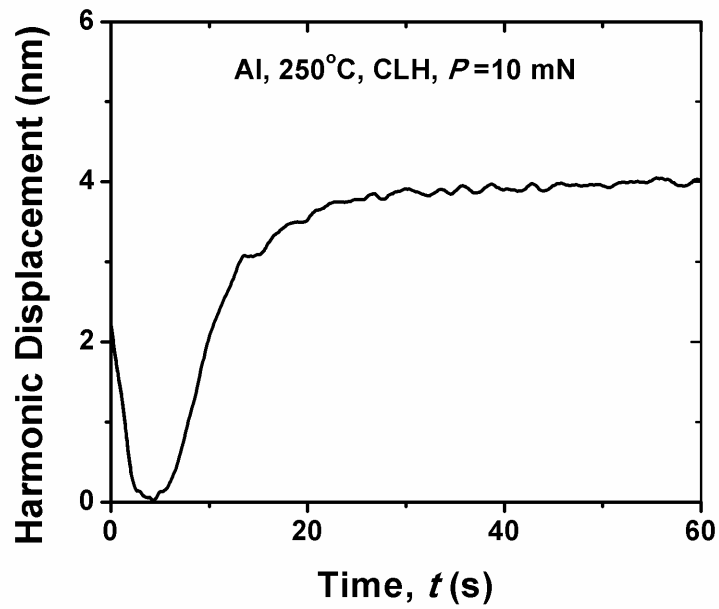
(b)

Figure 3.8. Basic data from constant load and hold indentation creep experiments with P = 10 mN for high purity aluminum at 250 °C: (a) the harmonic contact stiffness vs. time behavior; (b) the harmonic displacement vs. time behavior.
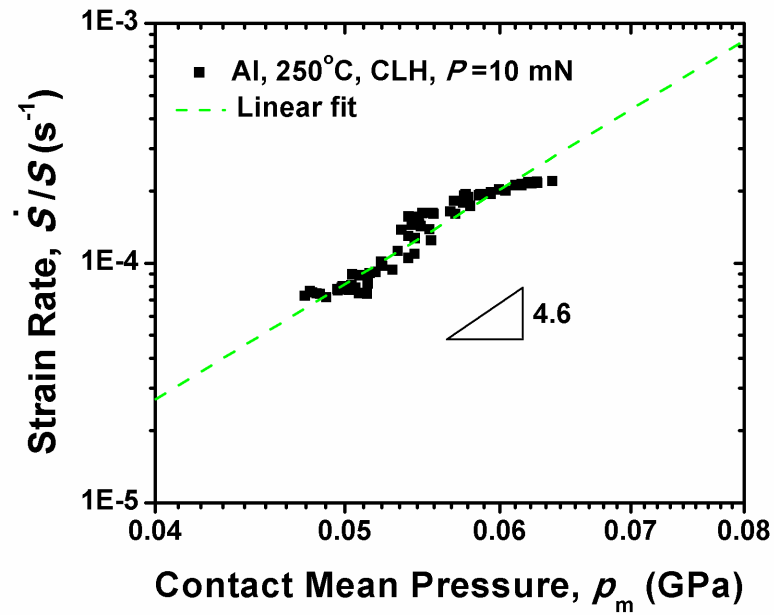
Figure 3.9. The data in Fig. 3.8 re-plotted as indentation strain rate vs. contact mean pressure on log-log axes.
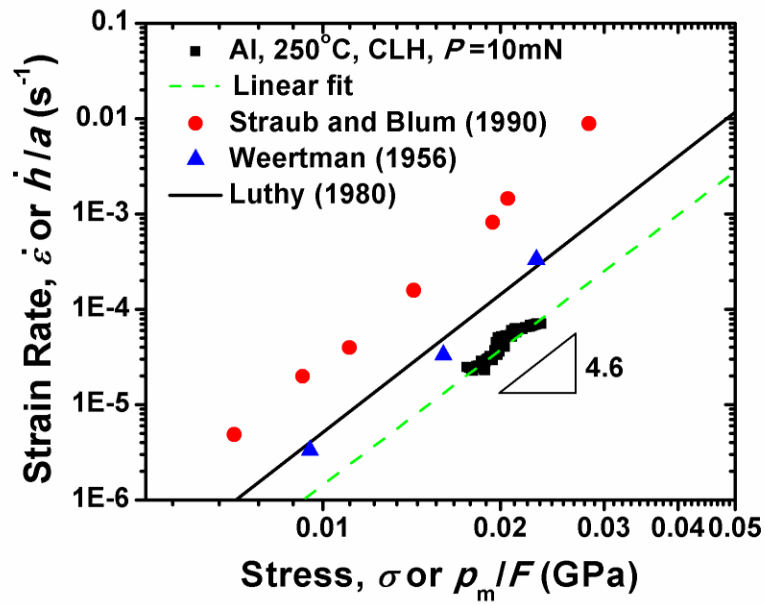
Figure 3.10. Comparison of the strain rate versus stress for high purity aluminum as determined by indentation creep and literature data at 250 °C. The indentation data assume that the creep exponent, n, is fixed at the measured value of 4.6.

Table 3.1. n and α of high purity aluminum from indentation and literature data at 250 $^{\circ}$C

Resource	Points in fit	n	α (units depend on n)
Indentation*	All data	4.6	1.04×10^{-38} Pa$^{-4.6}$s^{-1}
Straub & Blum	All data	5.4	4.37×10^{-43} Pa$^{-5.4}$s^{-1}
Weertman	All data	5.2	1.54×10^{-42} Pa$^{-5.2}$s^{-1}
Luthy**	All data	4.8	1.3×10^{-39} Pa$^{-4.8}$s^{-1}
Straub & Blum	Lowest 4 points	4.9	1.35×10^{-39} Pa$^{-4.9}$s^{-1}
Weertman	Lowest 2 points	4.4	6.64×10^{-37} Pa$^{-4.4}$s^{-1}

* The current investigation

** The line in Fig. 3.10 represents a curve fit to experimental data that has been normalized in a manner that allows the strain rate and stress to be calculated as a function of temperature.

CONCLUSION

New analysis methods have been developed to extract the constitutive uniaxial power-law creep parameters α and n from the load, displacement, time, and stiffness data recorded during an instrumented indentation creep experiment performed with a conical or pyramidal indenter. The methods are based on an analysis of Bower et al., which relates the indentation creep rate to the uniaxial creep parameters based on simple assumptions about the constitutive behavior. Experiments were performed using constant load and hold conditions (CLH), constant rate of loading conditions (CRL), and constant strain rate conditions (CSR). For the CLH and CRL methods, analytical, closed-form solutions for the displacement - time and load - displacement relationships are presented based on the following assumptions: a conical indenter tip geometry, a rigid, power-law creeping solid that is load history independent, and steady-state creep. For both loading methods, the theoretical displacement - time relations can be normalized to a form that is independent of the applied load or loading rate.

Building on the previous work of Bower *et al*., full-field finite element simulations were used to model the conical indentation of an elastic creeping solid to establish the influences of finite deformation and transients caused by elasticity. The results show that corrections to Bower's results for the pile-up/sink-in parameter, c, and the reduced contact pressure, F, are needed to account for finite deformation. The corrections are generally small but could be important in some experimental circumstances. Based on the finite element results, simple empirical equations are provided that relate c and F to the indenter angle, θ, and the measured stress exponent, n. The finite element simulations show that there is an initial transient in the indentation creep behavior resulting from the influences of elastic deformation. For constant load and hold indentation creep tests, the transient affects the evaluation of the stress exponent for penetration depths up to about ten times the elastic strain. Transient effects on the evaluation of α are more problematic and may extend to larger depths, especially for larger n.

The proposed methods were explored experimentally using amorphous selenium as a model material. Uniaxial compression and indentation creep tests were performed over

104

the temperature range of 25 ℃ to 40 ℃. Cylindrical selenium specimens compressed at high temperatures and low strain rates were found to deform stably into barrel-like shapes, while tests at low temperatures and high strain rates caused the sample to fail catastrophically. These results are consistent with the stress exponent and kinetic activation parameters extracted from nanoindentation creep tests using the proposed methods.

Direct comparison of uniaxial compression creep and indentation creep data obtained in amorphous selenium at 35 ℃ shows that the analysis of Bower et al. can be used to derive the basic uniaxial creep parameters α and n in $\dot{\varepsilon} = \alpha \sigma^n$ from indentation creep data. Although prior work has shown how n can be obtained, the results here show that it is also possible to measure the uniaxial creep coefficient α as well. The experimental results obtained in selenium also show that Bower's analysis correctly predicts the pile-up/sink-in parameter for a material with a stress exponent close to 1. The different indentation methods (CLH, CRL, and CSR) generate different results at short indentation creep times, but eventually the data from all three methods converge to a single strain rate-stress curve that is representative of steady state creep. The initial differences are attributed to a variety of factors including but not limited to elastic transients, the loss of geometric similarity, and power-law breakdown.

To combat the adverse affect of thermal drift, an alternative experimental technique and analysis method has been proposed to extract α and n from the elastic contact stiffness rather than the displacement. In applying this method, the indentation strain rate is defined as $\dot{S}/S$, which is equivalent to $\dot{h}/h$ in the limit of geometric similarity, meaning Bower's pile-up/sink-in parameter, c, must be constant with depth. When the measured displacement is not reliable, this condition can be confirmed by examining the extent that a plot of $\dot{S}/S$ versus p_m is linear. Experimental verification of the stiffness method is provided through constant load and hold indentation creep experiments performed with a Berkovich indenter on amorphous selenium at 35 ℃, in which thermal drift can be safely ignored because the entire experimental system is at thermal equilibrium. The 2-second load ramp in amorphous selenium generates a contact

geometry that initially exhibits significant pile-up followed by a gradual transition to sink-in behavior. Despite the loss of geometric similarity in the initial stages of creep, the recorded P, S, and t data can be used in conjunction with Sneddon's stiffness equation and Bower's analysis to accurately predict the projected contact area and uniaxial creep parameters α and n based on an assumed value of Young's modulus of the sample.

After experimental verification on amorphous selenium, the stiffness method was applied to high purity polycrystalline aluminum at 250 ℃. Localized heating of the sample created exceedingly large errors in the measured displacement due to thermal drift. Despite the large contribution from drift, however, direct comparison of previously published results and indentation creep data obtained in polycrystalline aluminum at 250 °C shows that Bower' analysis can be used to derive the basic uniaxial creep parameters α and n in $\dot{\varepsilon} = \alpha \sigma^{n}$. Although prior work has shown that it is possible to do this based on the measured load, depth, and time data recorded during an indentation creep test, the results here show that it is also possible to predict the creep properties using the measured elastic contact stiffness in a manner that is largely independent of thermal drift and the measured displacement.

VITA

Caijun Su was born in China in 1979. He was raised in Xiamen, China. After graduated from Tongan No. 1 High School, Xiamen, China in 1998, Caijun enrolled in the Department of Precision Instruments and Mechanology at Tsinghua University, Beijing, China, where he earned his Bachelor's and Master's Degree in Mechanical Engineering in 2002 and 2005. In 2005, he started to pursue a doctorate in Materials Science and Engineering at the University of Tennessee. He received a Ph.D. degree under the guidance of Dr. George M. Pharr in 2012.